

A model for permeability evolution during volcanic welding

Fabian B. Wadsworth¹, Jérémie Vasseur², Edward W. Llewellyn¹, Richard J. Brown¹,
Hugh Tuffen³, James E. Gardner⁴, Jackie E. Kendrick⁵, Yan Lavallée⁶, Katherine J. Dobson⁷,
Michael J. Heap⁸, Donald B. Dingwell², Kai-Uwe Hess², Jenny Schaubert⁶, Felix W. von Aulock⁶,
Alexandra R.L. Kushnir⁸, Federica Marone⁹

¹Department of Earth Sciences, Durham University, Durham, DH1 3LE, United Kingdom.

²Department of Earth and Environmental Sciences, Ludwig-Maximilians-Universität, 80333 Munich, Germany.

³Lancaster Environment Centre, Lancaster University, Lancaster, LA1 4YQ, United Kingdom.

⁴Department of Geological Sciences, Jackson School of Geosciences, 2305 Speedway Stop C1160, Austin, Texas 78712-1692, United States.

⁵School of Geosciences, University of Edinburgh, The King's Buildings, James Hutton Road, Edinburgh, EH9 3FE, Scotland.

⁶School of Environmental Sciences, University of Liverpool, Liverpool, L69 3BX, United Kingdom.

⁷Civil and Environmental Engineering, University of Strathclyde, Glasgow, G1 1XJ, United Kingdom.

⁸École et Observatoire des Sciences de la Terre, Université de Strasbourg, 5 rue de Rene Descartes, F-67084 Strasbourg, France.

⁹Swiss Light Source, Paul Scherrer Institute, 5232 Villigen PSI, Switzerland.

Volcanic ash and pyroclasts can weld when deposited hot by pyroclastic density currents, in near-vent fall deposits, or in fractures in volcano interiors. Welding progressively decreases the permeability of the particle packs, influencing a range of magmatic and volcanic processes, including magma outgassing, which is an important control on eruption dynamics. Consequently, there is a need for a quantitative model for permeability evolution during welding of ash and pyroclasts under the range of conditions encountered in nature. Here we present *in situ* experiments in which hydrous, crystal-free, glassy pyroclasts are imaged via x-ray tomography during welding at high temperature. For each 3D dataset acquired, we determine the porosity, Darcian gas permeability, specific surface area, and pore connectivity. We find that all of these quantities decrease as a critical percolation threshold is approached. We develop a constitutive mathematical model for the evolution of permeability in welding volcanic systems based on percolation theory, and validate the model against our experimental data. Importantly, our model accounts for polydispersivity of the grainsize in the particle pack, the pressures acting on the pack, and changes in particle viscosity arising from degassing of dissolved H₂O during welding. Our model is theoretically grounded and has no fitting parameters, hence it should be valid across all magma compositions. The model can be used to predict whether a cooling pyroclast pack will have sufficient time to weld and to degas, the scenarios under which a final deposit will retain a permeable network, the timescales over which sealing occurs, and whether a welded deposit will have disequilibrium or equilibrium H₂O content. A user-friendly implementation of the model is provided.

tuffisite; compaction; sintering; ignimbrite; synchrotron; experiment; magma

1. Introduction

Magma may fragment during ascent, forming volcanic ash and pyroclasts, which are subsequently transported in a gas phase. Following deposition the particles may weld – i.e. coalesce to form a

47 coherent material – if they remain hot enough to deform viscously. Welded deposits are observed in a
48 number of volcanic settings (Fig. 1). Subaerially, welded spatter deposits (Sumner et al. 2005; Sánchez
49 et al. 2012) and welded fall deposits (Houghton and Carey 2015) may form proximal to the vent, and
50 welding may occur in the depositional boundary layer at the base of a pyroclastic density current
51 (Branney and Kokelaar 2002) or after deposition and cessation of flow (Riehle 1973; Heap et al. 2014;
52 Lavallée et al. 2015). In the volcanic plumbing system, welding may occur in vent-filling ignimbrites
53 (Almond 1971), at conduit margins (Gardner et al. 2017; Wadsworth et al. 2020a), and in tuffisite veins
54 (Tuffen et al., 2003; Tuffen and Dingwell, 2005; Stasiuk et al. 1996; Kendrick et al. 2016; Kolzenburg
55 et al. 2019)) which are produced when gas–particle mixtures hydraulically fracture and intrude the
56 country rock or overlying/surrounding magma (Heiken et al. 1988; Stasiuk et al. 1996; Tuffen et al.
57 2003; Owen et al. 2019).

58 Welding is important because it leads to substantial changes in the physical properties of the deposit,
59 which transitions progressively from particulate to coherent (Branney and Kokelaar 1992), from
60 mechanically weak to mechanically strong (Kolzenburg et al. 2012; Vasseur et al. 2013), and from
61 permeable to impermeable (Colombier et al. 2017; Farquharson et al. 2017; Wadsworth et al. 2017b;
62 Kolzenburg et al. 2019; Heap et al. 2019). The effect on permeability is of particular interest because it
63 has been proposed that closure of outgassing pathways through tuffisites (Farquharson et al. 2017; Heap
64 et al. 2019) and clastic vent-filling deposits (Quane et al. 2009) can cause vent plugging and build-up
65 of gas pressure, leading to explosive eruption.

66 The physical process of welding of silicate melts is synonymous with *viscous sintering* as it is
67 understood in materials science research (e.g. Mackenzie and Shuttleworth 1949; Prado et al. 2001;
68 Wadsworth et al. 2016a); however, welding in natural environments presents added complications not
69 usually encountered in materials research. These include: (1) the particles may be supersaturated in
70 volatiles and therefore may degas during welding (Sparks et al. 1999; Wadsworth et al. 2019; Heap et
71 al. 2019); (2) the particles may be undersaturated in volatiles and undergo resorption during welding
72 (Sparks et al. 1999; Gardner et al. 2018); (3) the particles may be variably crystalline, or internally
73 porous (Quane and Russell 2005a; Wright and Cashman 2014; Heap et al. 2015; Kendrick et al. 2016);
74 and (4) the sintering pack of particles may be subjected to local stresses that promote shearing (e.g.
75 rheomorphism; Andrews and Branney 2011), or to substantial confining pressure (Sparks et al. 1999).
76 Furthermore, welding is strongly affected by the thermal pathway that particles follow after
77 fragmentation (Branney and Kokelaar 2002; Wadsworth et al. 2014, 2019; Kolzenburg et al. 2019;
78 Heap et al. 2019), which may be complex.

79 We develop a general model for evolution of permeability with time during welding of deposits of
80 crystal-poor volcanic particles, which we validate against experimental data. The important novelty
81 over previous work on welding dynamics (Riehle 1973; Riehle et al. 1995; Sparks et al. 1999; Quane
82 and Russell 2005a; Russell and Quane 2005; Lavallée et al. 2015) is that the model accounts for a range
83 of factors that complicate welding in volcanic systems: particle polydispersivity, non-isothermal
84 conditions, degassing of dissolved H₂O during welding, gas pressure, and confining pressure. The
85 model is therefore suitable for application to welding in a wide range of volcanic scenarios. We apply
86 our model to welding of rhyolites in a range of regimes, with the principal aim of exploring the
87 conditions under which a welded deposit is expected to preserve equilibrium degassed volatile
88 concentrations, the conditions under which disequilibrium volatile concentrations would be preserved,
89 and the conditions under which welding is arrested before permeability decreases to zero.

90 An implementation of the model is available via Vhub (<https://vhub.org/resources/4568>) and a
91 simplified version implemented in Excel™ is provided as Supplementary Material A brief practical
92 guide to its use is presented in Section 7.

93

94 2. Theoretical development

95 The welding of hot pyroclasts (above their glass transition temperature) is a specific case of viscous
96 sintering. In physical volcanology, ‘sintered’ has commonly been used as a descriptor for poorly or
97 incipiently welded deposits (Quane and Russell 2005b; Wright and Cashman 2014), but in materials
98 science, viscous sintering and volcanic welding are the same fundamental process, describing the
99 progressive coalescence of droplets toward a low-porosity, dense end-state. In this work we therefore
100 use the terms sintering and welding interchangeably. Welding is driven by stresses arising from surface
101 tension and confining stress (if applicable) and is opposed by the viscosity of the droplets and by
102 pressure in the interstitial gas phase. As welding progresses, the geometry of the pore space and the
103 degree of pore connectivity evolve, therefore causing the permeability to evolve. In this section, we
104 develop a mathematical model for the evolution of the permeability of welding, volatile-supersaturated
105 magmatic particles, building on previous models for the evolution of porosity of welding ash, and for
106 the relationship between permeability and porosity for particulate and percolating materials.

107

108 2.1 Evolution of porosity during welding

109 We adopt the model of Wadsworth et al. (2016a, 2017b, 2019), who treat the welding system as a
110 collection of unit cells that abstract the pore–particle system as a spherical ‘bubble’ of gas surrounded
111 by a shell of viscous melt; the gas is allowed to escape freely from the bubble, giving the model its
112 name: the ‘vented bubble model’ (Wadsworth et al., 2016). An overview of the main equations from
113 Wadsworth et al. (2019) is presented in this section; the reader is referred to the original work for their
114 derivation, solution, and experimental validation. The model gives the rate of change of the porosity
115 (i.e. gas volume fraction) ϕ with time t as a function of material properties:

$$\frac{d\phi}{dt} = -\frac{3\Delta P}{4\mu}\phi - \frac{3\Gamma}{2\mu a_i} \left(\frac{\phi_i}{1-\phi_i}\right)^{1/3} \phi^{2/3}(1-\phi)^{1/3}, \quad \text{Eq. 1}$$

116

117 where ϕ_i is the initial porosity, a_i is the initial radius of the ‘bubbles’, μ is the melt viscosity, Γ is the
118 surface tension, and ΔP is the difference between the squeezing isotropic pressure P acting on the
119 particles and the gas pressure in the bubbles P_g , such that $\Delta P = P - P_g$. In nature, ΔP is controlled by
120 a balance between the overburden pressure and the pore fluid pressure.

121 Eq. 1 can be presented in dimensionless form to facilitate collapse of experimental data over a range of
122 conditions, and to identify regimes of behavior (Wadsworth et al., 2019):

$$\frac{d\bar{\phi}}{d\bar{t}} = -\frac{3}{2} \left[\bar{P}\bar{\phi} + \left(\frac{1-\phi_i\bar{\phi}}{1-\phi_i}\right)^{\frac{1}{3}} \bar{\phi}^{\frac{2}{3}} \right], \quad \text{Eq. 2}$$

123

124 where, \bar{t} , \bar{P} , and $\bar{\phi}$ are, respectively, dimensionless time, pressure difference, and porosity. Time is
125 normalized by the capillary relaxation timescale $\lambda = \mu a_i / \Gamma$, pressure difference is normalized by a
126 reference capillary pressure scale $P_L = 2\Gamma/a_i$, and porosity is normalized by the initial porosity ϕ_i as
127 follows

128

129

130

$$\begin{aligned}\bar{t} &= \frac{t}{\lambda} = \frac{\Gamma}{a_i} \int_{t_i}^t \frac{1}{\mu} dt, \\ \bar{p} &= \frac{\Delta P}{P_L} = \frac{(P - P_g) a_i}{2\Gamma}, \\ \bar{\phi} &= \frac{\phi}{\phi_i}.\end{aligned}\tag{Eq. 3}$$

131

132 Melt viscosity is a strong function of temperature T , which may vary over time, and dissolved H₂O
 133 concentration C , which may vary with both time and spatial position within the particles if they are
 134 degassing during welding. This variation is accounted for by determining the spatial distribution of
 135 dissolved H₂O within the particles at each time via Fick's second law of diffusion, cast in spherical
 136 coordinates (Crank 1975), and computing the spatial average $\langle C \rangle$. The spatially-averaged viscosity $\mu =$
 137 $f(T, \langle C \rangle)$ is then used in the integral within the definition of \bar{t} , which runs from the time at which the
 138 welding starts t_i to the time-step of interest (Eq. 3).

139 The equations for the rate of porosity change – in dimensional form (Eq. 1) or dimensionless form (Eq.
 140 2) – can be integrated numerically to derive porosity change as a function of time $\phi(t)$ for welding
 141 particles. Wadsworth et al., (2019) describe a suitable numerical scheme and provide a user-friendly
 142 implementation for download. The full model accounts for particle polydispersivity, non-isothermal
 143 conditions, degassing during welding, and confining pressure. Polydispersivity of particles in the
 144 welding deposit manifests as a distribution of initial particle radii and interstitial pore radii. This is
 145 accounted for via convolution techniques discussed in Wadsworth et al., (2017b) and used here.

146

147 2.2 Evolution of permeability during welding

148 Section 2.1 presents a model for the evolution of porosity with time $\phi(t)$ in a welding deposit. We can
 149 extend this to derive a model for the evolution of Darcian permeability with time $k(t)$ by finding a
 150 constitutive relationship for $k(\phi)$. For sintering systems of particles, the most widely validated model
 151 is based on percolation theory (Martys et al. 1994; Wadsworth et al. 2016b):

$$k = \frac{2[1 - (\phi - \phi_c)]}{s^2} (\phi - \phi_c)^b \tag{Eq. 4}$$

152

153 where s is the specific surface area, ϕ_c is the percolation threshold, and b is a percolation exponent.
 154 For volcanic applications, this model has been validated for sintering glass spheres (Wadsworth et al.
 155 2017b, 2020b; Eichheimer et al. 2020), volcanic tuffisites (Heap et al. 2019), welded impact breccias
 156 (Heap et al. 2020), and for sintered volcanic fault gouge (Ryan et al. 2020a, b). Whereas k and ϕ are
 157 typically measured quantities, s is either measured or requires estimation, and ϕ_c and b are usually
 158 treated as fit parameters (e.g. Mueller et al. 2005; Colombier et al. 2017).

159 Wadsworth et al. (2016a) proposed that, from a micro-structural perspective, sintering systems of
 160 particles are a dynamic analogue of static overlapping sphere geometries, which are frequently used to
 161 consider the properties of low-porosity porous media (e.g. Martys et al. 1994). By drawing this analogy,
 162 we can use continuum percolation theory and simulation results to constrain b and ϕ_c , removing the
 163 need to fit for an unknown parameter. Based on theoretical arguments, the percolation exponent for
 164 overlapping sphere systems can be constrained to be $b = 4.4$ (Feng et al. 1987), which has been found
 165 to match both experimental and simulation data for overlapping spheres and systems of sintering
 166 particles (Vasseur and Wadsworth 2017). For monodisperse overlapping spheres, simulations show that

167 $\phi_c \approx 0.03$ (Kertesz 1981; Elam et al. 1984; Vasseur and Wadsworth 2017). These constraints are for
168 idealized sphere systems and require validation for sintering of non-spherical particles.

169 In our experimental campaign presented here (see Section 3), we can measure s directly. However, to
170 allow Eq. 4 to be applied in situations where s is not measured, we also test a constitutive model for
171 $s(\phi)$. By again drawing an analogy between dynamic sintering systems of particles and static
172 simulations of overlapping sphere domains, we can use a theoretical constraint for s (Torquato 2013)

$$s = -3(1 - \phi) \ln(1 - \phi) \frac{\langle a^2 \rangle}{\langle a^3 \rangle} \quad \text{Eq. 5}$$

173

174 where $\langle a^n \rangle$ is the n th moment of the distribution of pore sizes. Wadsworth et al. (2017c) provide a
175 method for predicting the distribution of pore sizes, and therefore $\langle a^n \rangle$, in sintering systems that have
176 a distribution of initial particle sizes.

177 The above framework provides a method by which $\phi(t)$ and $k(\phi)$ can be predicted. In regimes where
178 the permeability does not limit the gas escape and closure of the pore network by sintering (discussed
179 in Wadsworth et al. 2019), the time-dependence of permeability can then be computed *a priori* by
180 combining these two models, resulting in model predictions that can be tested against experiment.

181

182 3. Methods

183 3.1 Experiments and data analysis

184 We analyze the results from high temperature welding experiments using volatile supersaturated
185 rhyolitic obsidian particles, presented in Wadsworth et al., (2019). The rhyolite particles had a mean
186 size $\langle R \rangle = 2.33 \times 10^{-5}$ m, were polydisperse in grain size, and were crystal-free. The size distribution
187 of particles is reported in Fig. 2 along with $\langle R^n \rangle$ for $n \leq 3$.

188 The rhyolite particles were packed into free-standing cylinders 3 mm high using a compression forming
189 method (Wadsworth et al. 2016b) and were heated using a laser heating system (Fife et al. 2012).
190 Temperature was monitored using a calibrated pyrometer and additional calibration steps (see
191 Wadsworth et al. 2017b). Temperature fluctuations were greater than the absolute uncertainty on
192 temperature and were maximally ~ 5 K (i. e. ± 2.5 K). Four runs were performed, in which the packed
193 free-standing cylinders were heated at $0.067 \text{ K} \cdot \text{s}^{-1}$ to temperatures $T = 1053, 1144, 1217$ and 1248
194 K. The experiments were performed *in situ* at the TOMCAT beamline of the Swiss Light Source and
195 imaged simultaneously via x-ray computed tomography, resulting in a time-series of 3D reconstructions
196 of the evolving geometry of the particle pack throughout the welding process. Full 3D scans were
197 collected at intervals between 1 and 107 s with a spatial resolution of $1.7 - 2.0 \mu\text{m}$ voxel edge lengths.
198 The initial H_2O concentration was 0.14 wt.% (Wadsworth et al. 2019).

199 A sub-set of the 3D datasets in each run were segmented to reconstruct the non-pore volume (i.e. the
200 volume of the welding particle phase) and the pore volume between the particles, using Avizo™ using
201 an auto-thresholding algorithm. A time-series of representative images of segmented volumes are
202 shown in Fig. 3. The porosity ϕ is calculated directly from the tomography data as the ratio of the
203 measured pore volume to the total volume (non-pore volume plus pore volume). The pore volume is
204 divided into connected porosity ϕ_p (i.e. pores and pore networks that connect across at least one
205 opposite face of the measured domain) and isolated porosity, such that the isolated porosity is $\phi - \phi_p$.
206 Using a range of suitable segmentations, we determine the uncertainty on the porosity to be
207 approximately 0.5% of the stated values. This is a conservative estimate based on variations in the
208 segmentation thresholds used. During welding, the pore volume decreases and the sample shrinks (Fig.

209 3a-c). The pore space is initially fully connected (Fig. 3a) but develops domains that are isolated (Fig.
 210 3b) as welding progresses. The stable end-state is a melt continuum containing isolated bubbles (Fig.
 211 3c); the topological inverse of the initial state (Fig. 3a).

212 In this study we use these tomography data – results from which are presented in Wadsworth et al.
 213 (2019) – to determine the permeability of the samples through the welding process. The segmented pore
 214 volume is used as the input for LBflow, a numerical package for simulating fluid flow using the lattice-
 215 Boltzmann method (Llewellyn 2010a, b). LBflow discretizes the pore volume into a cubic lattice of fluid
 216 nodes, to which we add a periodic boundary and a buffer zone to allow flow to connect across faces,
 217 and simulates fluid flow under an applied body force, equivalent to applying a pressure gradient across
 218 the sample. We simulate the flow of air at ambient conditions (fluid viscosity $\mu_f = 1.8205 \times$
 219 10^{-5} Pa.s and density $\rho_f = 1.2047$ kg.m⁻³) under a uniform fluid pressure gradient of
 220 $\nabla P_f = 10^{-2}$ Pa.m⁻¹. The fluid velocity u is read out at every node and the average fluid velocity $\langle u \rangle$
 221 is computed. We run the simulation until $\langle u \rangle$ stabilizes to a steady state value, and ensure the flow is
 222 always in the low-Reynolds number (i.e. creeping flow) regime (for more details, see Llewellyn, 2010b).
 223 Visualizations of computed fluid flow lines through representative segmented volumes are shown in
 224 Fig. 3. The permeability is calculated using Darcy’s law for each 3D dataset:

$$k = -\frac{\mu_f}{\nabla P_f} \langle u \rangle \quad \text{Eq. 6}$$

225

226 The specific surface area s for each the 3D dataset is determined using a ‘marching cubes’ algorithm
 227 (Lorensen and Cline 1987; Lewiner et al. 2003). This algorithm extracts an isosurface for the pore–
 228 particle walls in the 3D datasets. Normalizing the area of the surface by the volume of the sample or
 229 domain gives s (in units of m⁻¹). Using 3D datasets segmented using different segmentation threshold
 230 choices, we estimate the uncertainty on the permeability to be 10^{-17} m² based on the convergence
 231 criterion used in LBflow. The uncertainty on our surface area determination is approximately 0.8%.
 232 This uncertainty is determined by computing the standard error on repeat measurements of surface area
 233 on different sub-volumes selected in domain.

234

235 3.2 Numerical modelling

236 We solve Eq. 2 numerically, following Wadsworth et al. (2019), to obtain $\bar{\phi}(\bar{t})$, which we
 237 dimensionalize for each experiment via the relationships in Eq. 3, and the material parameters μ , Γ ,
 238 $\langle a_i \rangle$, and ϕ_i . Calculating μ requires the spatial distribution of dissolved H₂O in the particles at every
 239 timestep throughout the welding process, which we compute via Fick’s second law, following
 240 Wadsworth et al. (2019). We then integrate across the measured particle radii to find a spatially
 241 averaged viscosity and convolve this with the initial particle size distribution (Fig. 2) to arrive at a
 242 global average of the viscosity for the population of particles used – termed $\langle \mu \rangle$. We use constitutive
 243 models appropriate for rhyolitic liquids: viscosity $\mu(T, C)$ from Hess and Dingwell, (1996); H₂O
 244 diffusivity $D(T, P_g, C)$ from Zhang and Ni, (2010); and the equilibrium H₂O solubility at the particle
 245 boundary $C_e(T, P_{\text{H}_2\text{O}})$ from Liu et al., (2005), where $P_{\text{H}_2\text{O}}$ is the partial pressure of H₂O in the pore
 246 space. For our experiments $P = 0.1$ MPa, and we use $P_{\text{H}_2\text{O}} = 0.1P_g$ to account for standard laboratory
 247 humidity (Von Aulock et al. 2017). We use $\Gamma = 0.3$ N.m⁻¹ for nominally dry silicate melts (Parikh
 248 1958). The average initial pore radius $\langle a_i \rangle$ for the experiments is determined using Wadsworth et al.
 249 (2017b), and the starting porosity ϕ_i is taken directly from segmented tomography data.

250

251 4. Results and analysis

252 Our results and analysis comprise three parts. First, we validate the $s(\phi)$ model (Eq. 5; Section 2.2)
253 against the values determined from the tomographic data. Second, we compare the $k(\phi)$ model (Eq. 4;
254 Section 2.2) with $k(\phi)$ data from the LBflow simulations of the *in situ* data, for which all quantities are
255 measured directly. Third, we validate the $k(t)$ model (i.e. the combined $k(\phi)$ and $\phi(t)$ models (Eqs 1-
256 3; Section 2.1)) against $k(t)$ data from the LBflow simulations.

257

258 4.1 The specific surface area during welding $s(\phi)$

259 The specific surface area s measured during welding in the evolving *in situ* datasets varies non-linearly
260 with ϕ . In Fig. 4 we show the measured s values compared with the model (Eq. 5; Section 2.2). When
261 solving the model we use the moments of a polydisperse pore size distribution calculated from a
262 polydisperse overlapping sphere model used for sintering problems (Wadsworth et al. 2017d), which
263 uses the particle size distribution (Fig. 2) and the initial porosity ϕ_i as input values. In the case of the
264 data presented here, the pore size distribution moments are $\langle a \rangle = 8.01 \times 10^{-6}$ m, $\langle a^2 \rangle = 9.40 \times$
265 10^{-11} m², and $\langle a^3 \rangle = 1.35 \times 10^{-15}$ m³. With no fitting parameters, the data and the model agree with
266 a coefficient of determination of $r^2 = 0.8$.

267 We hypothesize that the deviation between the model and the data at high porosity is attributable to the
268 initial angularity of the particles, consistent with the observation that initially-spherical particles do not
269 show this discrepancy during sintering (Wadsworth et al. 2017b), and that the data approach the model
270 more closely as the particles progressively round during welding. The magnitude of the deviation
271 between the measured and the predicted s taken at the initial packing porosity – termed Δs_i – can be
272 used to estimate the excess surface. We find that $\Delta s_i \langle a_i \rangle \approx 0.2$, which implies that the surface is
273 approximately 20% greater than it would be for a pack of spherical particles with the same size
274 distribution. A sphere has a single radius of curvature and, for a given volume, a sphere has the lowest
275 surface area of any object. Any solid object of the same volume that has a higher surface area must
276 necessarily have non-uniform surface curvature which includes regions with smaller radius of curvature
277 than a sphere. In order to find a conservative estimate for the minimum radius of curvature for such an
278 object, we consider a prolate spheroid with the same volume as a sphere of radius a , but a surface area
279 that is 20% higher. Such a spheroid has major semi-axis $c \approx 2.16a$ and minor semi-axes $m \approx 0.68a$.
280 The minimum radius of curvature of the spheroid is $m^2/c \approx 0.21a$ (at each pointed end); hence an
281 object with a surface area that is 20% larger than a sphere of the same volume must have at least one
282 radius of curvature that is no larger than 21% of the sphere's radius.

283 We can use this information to estimate the maximum time taken for the irregular particles in our
284 experiments to round under the action of surface tension. The timescale for relaxation of a surface
285 irregularity with radius of curvature ξ is given by $\lambda_\xi = \xi\mu/\Gamma$ (Wadsworth et al. 2017a). For $\xi =$
286 $0.21\langle a_i \rangle = 1.68 \times 10^{-6}$ m, the rounding time for our experiments at 1248 K is $\lambda_\xi = 126$ seconds. In
287 our data, the porosity at which $t = \lambda_\xi$ is met is approximately at a porosity of $\phi \approx 0.4$, which is
288 consistent with the porosity at which Δs_i approaches zero and the model and data coincide (Fig. 4).
289 This implies that particle irregularity may only be important during the very initial stage of welding,
290 and becomes irrelevant quickly. We propose that this simple test supports the hypothesis that initial
291 surface angularity of the particles is responsible for the deviation from the model for specific surface at
292 high porosities. We conclude that, for the case of initially angular particles, our model becomes more
293 valid as welding progresses. Empirical adjustments could be made to the model for $s(\phi)$ to account for
294 angularity (e.g. by adjusting the moments of the pore size distribution by an empirical factor).

295

296 4.2 The relationship between permeability and porosity $k(\phi)$

297 The permeability of the samples determined through fluid-flow simulations depends strongly on
298 porosity (Fig. 5a – note the logarithmic scale for k). Permeability varies by two orders of magnitude
299 over the porosity interval $0.1 \leq \phi \leq 0.6$ and, at the lowest porosities, simulations show that the samples
300 are impermeable (i.e. $k = 0$). Fig. 5a also plots the theoretical $k(\phi)$ relationship in Eq. 4 using the
301 model for $s(\phi)$ from Eq. 5 (see Section 4.1), $b = 4.4$, and $\phi_c = 0.03$. This shows a generally good
302 match to the data.

303 Improvements in the fit of $k(\phi)$ (Eqs 4 & 5) could be made if ϕ_c and b were treated as fitting
304 parameters. In the inset to Fig. 5a, we perform a minimization exercise in which we allow ϕ_c and b to
305 vary. Our minimization parameter is the sum of the square residuals between the data and the model
306 result, where we define the residuals on the basis of the Deming approach in which both the mismatch
307 in k and ϕ are accounted for. The coefficient of determination is then the ratio of this sum of square
308 residuals for a given ϕ_c and b combination, and the total variance in the data. In the inset to Fig. 5a, we
309 show the results of this fitting exercise, demonstrating that the best-fit combinations of ϕ_c and b co-
310 vary, such that the residual function has a trench-like minimum. In Fig. 5a, we show a grey band, which
311 bounds all solutions to Eq. 4 for which the coefficient of determination is within 2% of the absolute
312 best fit pair of ϕ_c and b . We note that this 2% variation in the fit quality encompasses the theoretically-
313 grounded values $\phi_c = 0.03$ and $b = 4.4$, derived for monodisperse packs of spherical particles. Based
314 on this analysis, we conclude that: 1) the quality of the model fit to the $k(\phi)$ data is not sensitive to
315 small variations ($\pm 2\%$) in the best-fit parameters; and 2) that the theoretically-grounded values of the
316 fit parameters remain valid for packs of natural volcanic particles, despite violation of the monodisperse
317 and spherical assumptions. We therefore adopt $\phi_c = 0.03$ and $b = 4.4$ as empirically-validated,
318 theoretically-grounded constants.

319 Due to the *in situ* nature of our experiments, we extract the connected porosity ϕ_p directly. If we then
320 look at the connectivity of the pore space ϕ_p/ϕ (as defined in Colombier et al. 2017) as a function of
321 ϕ during welding, we would predict that this metric would fall to zero as $\phi \rightarrow \phi_c$ during welding. The
322 value $\phi_c = 0.03$ is consistent with the observed drop in connected porosity (Fig. 5b).

323 The data indicate that there is no strong dependence of the $k(\phi)$ trend with temperature, or the thermal
324 path taken to reach the peak temperature. This is consistent with Eqs 1-4 which predict that, while
325 temperature controls the time-evolution of permeability, it does not influence the path of the
326 permeability–porosity relationship. Minor anisotropy in the permeability at the beginning of the
327 experiment (e.g. at high porosity) appears to grow at low porosities (observe the divergence of k_x with
328 respect to k_z as $\phi \rightarrow \phi_c$, in Figure 5a), which could be attributed to minor effects of the compression-
329 packing method of sample preparation. No anisotropy is predicted by the model approach (Section 2).

330

331 4.3 Time-evolution of permeability $k(t)$

332 With a validated constitutive law for $k(\phi)$ (Eqs 4-5), we can combine our model for $k(\phi)$ with the
333 vented bubble model for $\phi(t)$ (Eqs 1-3), giving a method for calculating the time-dependence of
334 permeability during welding $k(t)$. Fluid flow simulations through the segmented 3D datasets from our
335 *in situ* experiments yield $k(t)$ data, which we plot in Fig. 6. The data show that permeability drops
336 during welding, and drops more rapidly at higher temperature.

337 In Fig. 6 we also show our model results in which the model for $s(\phi)$ (Eq. 5; Fig. 3) is used to solve
338 the model for $k(\phi)$ (Eq. 4) using $\phi_c = 0.03$ and $b = 4.4$ (see Section 4.2; Fig. 5). This solution for
339 $k(\phi)$ is then mapped to each t by first solving the dimensionless universal form of the vented bubble
340 model (Eq. 2) and then rendering that solution dimensional via Eq. 3 and the constitutive equations for
341 the material used here (Section 3.2). The validation of this model for $\phi(t)$ is presented in detail
342 elsewhere for these same experiments (Wadsworth et al. 2019) and not restated here. The model and

343 the data agree well. For comparison, we also show what the model solution would be if we did not
344 account for the diffusive degassing of the particles during sintering, and had instead assumed either the
345 initial or equilibrium H₂O concentration in the glass throughout (Fig. 6). Neglecting diffusive degassing
346 of the particles provides a very poor description of the data and confirms that, for our experimental
347 conditions, accurate prediction of permeability during welding requires that degassing is accounted for.

348

349 5. Discussion

350 The results in Section 4 constitute an experimental validation of the workflow for modelling $k(t)$ via
351 separate models for $\phi(t)$, $s(\phi)$, and $k(s, \phi)$. The model accounts for syn-welding pyroclast degassing
352 and the associated change in pyroclast viscosity, contains no empirical adjustments, and is grounded in
353 percolation and sintering theory. This means that, once validated in a given regime (e.g. low \bar{P}), it can
354 be extrapolated and applied to conditions or compositions, within that regime, beyond those for which
355 it was specifically validated. In this section, we test the extent to which we have indeed validated this
356 model and state the conditions that would require further validation.

357

358 5.1 Toward a general model for permeability and permeability evolution in welding systems

359 The data collected here are for a specific composition, particle size distribution, and thermal treatment.
360 In order to test the extent to which our model results for $s(\phi)$, $k(s, \phi)$, and $k(t)$ can be applied more
361 generally, we can compare our model with other available data for those quantities. The data used for
362 this comparison are summarized in Table 1. To compare across a range of material properties and
363 experimental or simulation conditions, it is convenient to use the dimensionless form of our models.

364 The $\phi(t)$ model (Eq. 1) is already presented in dimensionless form $\bar{\phi}(\bar{t})$ (Eqs. 2 and 3) and has been
365 validated extensively over a range of conditions (Wadsworth et al. 2016a, 2017b, d, 2019).

366 We non-dimensionalize the specific surface area s by the moments of the pore size distribution (see
367 Section 4.1), giving $\bar{s} = s\langle a^3 \rangle / \langle a^2 \rangle$ for the polydisperse case, and $s\langle a \rangle$ for the monodisperse case. The
368 model (Eq. 5) reduces to the dimensionless form $\bar{s} = -3(1 - \phi) \ln(1 - \phi)$, which is shown in Figure
369 7a, along with data from this study, literature data from sintering anhydrous spherical glass beads using
370 the same *in situ* technique (Wadsworth et al. 2017b), and literature data from simulations of overlapping
371 sphere packs (Vasseur and Wadsworth 2017; Vasseur et al. 2020) where $\langle a^3 \rangle / \langle a^2 \rangle$ or $\langle a \rangle$ are computed
372 following the same technique as used here (Torquato 2013; Wadsworth et al. 2017d). Data are presented
373 in Table 1. Despite the very different pore size and particle size distributions in these studies, the
374 collapse to the dimensionless $\bar{s}(\phi)$ model is generally reliable. We note that some samples from
375 Wadsworth et al. (2017b) have \bar{s} that deviate from the model, which is likely to be due to heterogeneity
376 in the initial polydisperse packing. The discrepancy between our data and the model at high ϕ was
377 noted in Section 4.1, and attributed to particle angularity. The literature data, which are for systems of
378 spheres, show closer agreement at high ϕ , which is consistent with that hypothesis. This additionally
379 supports the conclusion that welding systems are indeed microstructural analogues of overlapping
380 particle domains. Across all datasets, we find reasonable agreement with our model (Fig. 7a) with a
381 global goodness of fit of $r^2 = 0.80$.

382 We non-dimensionalise the permeability k by a reference permeability $k_r = 2(1 - (\phi - \phi_c)) / s^2$,
383 giving $\bar{k} = k / k_r$. The model (Eq. 4) reduces to the dimensionless form $\bar{k} = (\phi - \phi_c)^b$, which is shown
384 in Figure 7b, along with data from this study, and literature data from studies using samples which were
385 (or are inferred to have been) initially particulate and which have undergone welding: sintered soda-
386 lime-silica glass beads from Wadsworth et al., (2017a), which were also welded using the same *in situ*
387 technique; glass beads welded *ex situ* (Blair et al. 1993; Wadsworth et al. 2020b; Eichheimer et al.

388 2020); obsidian welded *ex situ* (Okumura and Sasaki 2014); welded crystal-bearing andesite particles
389 (Kendrick et al. 2016); and natural welded systems for which s is constrained (Heap et al. 2015, 2019;
390 Ryan et al. 2020a). Where the original study does not give a value for s , we calculate it using Eq. 5.
391 Data are presented in Table 1. Across this range of experimental-to-natural variability, we find
392 reasonable agreement with our model (Fig. 7b) with a global goodness of fit of $r^2 = 0.94$.

393 Finally, in Fig. 7c, we test our $k(t)$ model against previous data. We compare the results from this study
394 with those from Wadsworth et al. (2017a) in which soda-lime-silica glass beads were sintering *in situ*,
395 yielding a similar time-dependent description of the permeability. Due to subtle differences in the initial
396 packing and the random close packing difference between spherical and angular particles, the initial
397 value of \bar{k} , termed \bar{k}_i , from which each specific experiment starts the process is different. For any given
398 \bar{k}_i , there will be a different model result in $\bar{k}(t)$. Therefore, to provide a common basis that allows us
399 to compare data and model results across all conditions, we use \bar{k}/\bar{k}_i , which we note is equivalent to
400 k/k_i (i.e., the k_r terms cancel). Note that this normalization step does not affect the generality of Eq.
401 4, but is simply a device to allow all of the data to be compared to a single, master curve.

402 The dimensionless time \bar{t} is defined in Eq. 3 and is specific to the temperature–time pathway taken. For
403 the anhydrous soda-lime-silica glass beads, there is not the additional requirement to account for the
404 degassing of H_2O , which is accounted for in the sintering obsidian particles analyzed herein
405 (Wadsworth et al. 2019). When cast in this space (Fig. 7c), the model given in Eq. 4 becomes $\bar{k}/\bar{k}_i =$
406 $[(\phi - \phi_c)/(\phi_i - \phi_c)]^b$ and, following the same principles as is shown dimensionally in Fig. 6, the
407 time dependence for $\bar{\phi}(\bar{t})$ is used together with $k(\phi)$ to predict $\bar{k}(\bar{t})$. For the sintering of soda-lime-
408 silica glass beads, we use the monodisperse form of this model, because the beads were sieved to a
409 single size fraction, while for the data presented herein, we use the polydisperse model presented here.
410 This difference results in two different model curves. The agreement between the models and these two
411 datasets leads us to conclude that, while the particle angularity played a minor but measurable role in
412 controlling $s(\phi)$, it does not strongly influence the dynamics of permeability decrease. Similarly, this
413 suggests that degassing and the associated evolution of viscosity gradient in the particles does not
414 substantially alter the evolution of the microstructure and so does not appear to impact the permeability
415 decay when accounted for via the approach of Wadsworth et al. (2019).

416

417 5.2 Successes and limitations of our model and validation

418 The *in situ* nature of the data allows us to determine s , ϕ , and k , independently, as functions of measured
419 experimental time t ; hence to validate, independently, our models for $s(\phi)$ (Fig. 4), $k(\phi)$ (Fig. 5), and
420 $k(t)$ (Fig. 6). In each case we find reasonable agreement between model and experiment.

421 The principal limitation to the model validation is associated with the parameter \bar{P} (Eq. 3). Wadsworth
422 et al. (2019) showed that Eqs 1-3 are valid descriptions of $\phi(t)$ during welding, even when confining
423 pressure exceeds the Laplace surface pressure – i.e. when $\bar{P} > 1$ and validated up to $\bar{P} = 100$. However,
424 this does not necessarily confirm that the *combination* of $\phi(t)$ and $k(\phi)$, to determine $k(t)$, would also
425 be valid at higher confining pressures. It could be that the so-called pressure sintering regime at $\bar{P} > 1$,
426 induces particle–particle flattening sufficient to change the microstructure such that the analogy with
427 static percolation theory developed for overlapping spheres, which underpins our $k(\phi)$ model, is no
428 longer applicable. For instance, as \bar{P} increases above unity, the sintering rate increases (Rahaman and
429 De Jonghe 1990; Ryan et al. 2018; Wadsworth et al. 2019), and it would be reasonable to assume that
430 the microstructural evolution would be different as slow, capillary-driven processes, such as neck
431 formation and pore geometry smoothing, become negligible on the timescale of porosity decay. We
432 therefore consider that our model is validated only for $0 < \bar{P} < 1$, and validation of $k(\phi, t)$ at higher
433 \bar{P} should be a topic for future investigation. Nevertheless, the low \bar{P} regime is relevant to a range of

434 volcanic scenarios (Gardner et al. 2018, 2019; Wadsworth et al. 2019; Heap et al. 2019). Similarly, we
435 have not provided a tensorial description of Eq. 4 that would allow permeability anisotropy to be
436 predicted under stresses that give rise to shear deformation. However, syn-welding shear is clearly
437 preserved by textures in volcanic deposits (Fig. 1; c.f. Andrews and Branney 2011), so the development
438 of anisotropy of permeability during welding under shear is another priority for future investigation.

439 There are further complexities that may arise during welding in nature that are not accounted for in our
440 model. For example, in Fig. 1 we show that clasts in tuffisites or ignimbrites may be internally porous
441 (e.g. pumice and fiammé), or variably crystalline (e.g. lithics). Additionally, welding packs may be
442 heterogeneous, composed of particles with a range of compositions, representing a range of provenance
443 pre-deposition (Saubin et al. 2016) or variable alteration during transport or gas flow (Berlo et al. 2013;
444 Casas et al. 2019; Paisley et al. 2019), and the pore space can be in-filled with vapor-phase deposition
445 or expanded by leaching of pore walls (Schipper et al. 2015). This kind of diversity of clast types and
446 evolution of pore geometries in natural systems could be accounted for in a model that convolves Eqs
447 1-3 with a distribution of clast rheology, which in turn could be rendered time-dependent in a similar
448 manner to our quantitative account of degassing which leads to a time-dependent particle rheology.
449 However, we have not validated those effects here, nor has the impact of these effects on the
450 permeability been tested, and it is possible that a wide distribution of particle rheology has a non-trivial
451 impact on the $k(t)$ pathway taken during welding.

452 As a coarse test of the impact of the complexities discussed above, we show that our $k(\phi)$ model is
453 effective across a wide range of natural samples collected from systems that sintered under a wide range
454 of conditions (Fig. 7b). For example, the sintered tuffisite materials from Heap et al. (2019) and the
455 volcanic gouge sintered in the solid-state from Ryan et al. (2020) are both shown to have formed at
456 appreciable confining pressure. Heap et al. (2019) show that the wall of their studied tuffisites host an
457 equilibrium value of 0.46 wt.% H₂O, while the far-field hosts an equilibrium value of 1.04 wt.% H₂O,
458 and that these limits are bridged by a diffusion profile toward the tuffisite. Assuming that the wall value
459 would be in equilibrium with the gas at the vapor pressure in the tuffisite (and we assume that this value
460 was approximately constant), and that the far-field value would be in equilibrium with the liquid at
461 magmatic pressure, we can estimate \bar{P} for this tuffisite. Using a solubility model (Liu et al. 2005) we
462 find that the wall value relates to $P_g \approx 2$ MPa and that the far-field value relates to $P \approx 9$ MPa, resulting
463 in $\Delta P \approx 7$ MPa. Given the constraints on P_L from Heap et al. (2019), we therefore estimate that $\bar{P} \approx$
464 116 for that tuffisite. Despite the high \bar{P} regime and the polymictic nature of the tuffisite fill, the
465 permeability–porosity relationship collapses to our general description to within less than an order of
466 magnitude deviation in k from our model at any porosity (Fig. 7b). We propose that such a collapse in
467 $k(\phi)$ space is a reasonable indication that, while the effects discussed above may influence pore
468 geometries, this does not appear to translate into a substantial difference in the hydraulic properties of
469 these rocks.

470

471 **6. Applications and regimes in natural welding**

472

473 **6.1 Degassing regimes in natural rhyolite welding**

474 We can apply our experimentally validated model to investigate volcanic welding with syn-welding
475 degassing. Here, we investigate welding in a rhyolite ash pack with an initial water concentration C_i ,
476 initial monodisperse particle size R , isothermal temperature T , and initial packing porosity ϕ_i , using
477 our model to predict the evolution of permeability with time, and the time it takes for the permeability
478 reach zero (i.e. the time at which $\phi < \phi_c$). We explore the scenario where $T = 1100$ K, which
479 represents an insulated magmatic temperature (cooling is discussed later), and an initial porosity $\phi_i =$
480 0.5, which is typical of loose randomly packed angular particles (e.g. Fig. 5). We vary C_i and R over a

481 wide range representative of silicic systems: $0.1 < C_i < 5$ wt.%, and $10^{-6} < R < R_c$ m, where $R_c =$
 482 $\sqrt{\Gamma/(\rho g)}$ is the radius above which gravitational effects dominate the particle deformation over surface
 483 tension effects, $\rho \approx 2000$ kg. m⁻³ is the rhyolite particle density (Lange and Carmichael 1987), and g
 484 is the acceleration due to gravity. For rhyolites, $R_c \approx 4 \times 10^{-3}$ m, such that particles smaller than this
 485 value will not deform under their own mass. We assume that welding is occurring at $P_g = 0.1$ MPa
 486 vapour pressure at the Earth's surface, simulating welding in very shallow tuffisites or at the base of
 487 hot pyroclastic density currents. We confine our analysis to the low- \bar{P} regime (discussed above). At
 488 these conditions, the solubility model we used for our experimental validation predicts that the
 489 equilibrium water concentration is $C_e = 0.1$ wt.% (Liu et al. 2005), which, given sufficient time, is the
 490 value to which the particles will degas by diffusion.

491 In Fig. 8, we show indicative model results. We find that when the initial water concentration C_i is close
 492 to or equal to the equilibrium value (e.g. initial supersaturation is low or zero), the permeability during
 493 welding decays smoothly. In this case packs with larger particle radius will both (1) start from a higher
 494 initial permeability, and (2) take longer to weld to zero permeability (Fig. 8a). When the initial water
 495 concentration is much higher than the equilibrium value, such that $C_i \gg C_e$, we find more complex
 496 welding pathways can be taken in $k(t)$ space, depending on particle radius. We find three
 497 phenomenological regimes; to demonstrate these regimes, we use the example of $C_i = 1$ wt.% (Fig.
 498 8d).

- 499 (1) For relatively small particles ($R = 10^{-5}$ m in this example) permeability decay is almost
 500 indistinguishable from the case where $C_i = C_e$ (Fig. 8a). Inspection of the evolution of the
 501 spatially-averaged H₂O concentration $\langle C \rangle(t)$ (Fig. 8e) demonstrates that this is because $\langle C \rangle$
 502 falls rapidly to C_e , before appreciable welding has occurred: i.e. degassing is efficient on the
 503 timescale of welding. Consequently, the particles have equilibrium H₂O concentration for the
 504 majority of the welding process, and the final outcome is expected to be a deposit that is fully
 505 degassed when welding is complete.
- 506 (2) For relatively large particles ($R = 10^{-3}$ m in this example) permeability decays much more
 507 rapidly than for the case where $C_i = C_e$, and more rapidly even than the smaller particles
 508 discussed in (1) above. Inspection of $\langle C \rangle(t)$ demonstrates that this is because H₂O concentration
 509 remains close to C_i throughout most of the welding process: i.e. degassing is inefficient on the
 510 timescale of welding. Consequently, the viscosity of the particles is much lower than for the
 511 equilibrium case, leading to faster welding. The final outcome is expected to be a deposit that
 512 retains disequilibrium H₂O concentration when welding is complete.
- 513 (3) For particles of intermediate size ($R = 10^{-4}$ m in this example) the permeability decay is more
 514 complex, with a pronounced inflection during welding. This is because degassing and welding
 515 operate over similar timescales, and the increase in viscosity that occurs as the particles degas
 516 leads to an appreciable decrease in welding rate as welding progresses. Depending on the exact
 517 conditions, the final deposit will have a water content between C_i and C_e when welding is
 518 complete.

519 To explore these regimes further, we consider the total time taken for welding to complete λ' for
 520 particles of different size and initial H₂O concentration. We take λ' as the time elapsed when ϕ reaches
 521 ϕ_c . In Fig. 9 we plot λ' as a function of the starting particle radius, showing the solution for a wide
 522 range $C_e \leq C_i \leq 5$ wt.%, for rhyolitic particles welding at 1100 K and $P_g = 0.1$ MPa. We observe that,
 523 for a given C_i , the welding time changes with particle size, and passes through three regimes,
 524 corresponding to regimes (1) – (3) above. In regimes (1) and (2), welding time increases with particle
 525 size, but welding time in regime (2) may be lower than welding time in regime (1), despite larger particle
 526 size, if H₂O concentration is sufficiently high. In regime (3), at intermediate particle size, welding time
 527 decreases as particle size increases.

528 These 3 regimes can be understood by considering the capillary Peclet number Pc (Gardner et al. 2018),
 529 which compares the timescale for diffusive degassing λ_D with the timescale for welding in the low-
 530 \bar{P} regime, λ (Eq. 3). The diffusive timescale is $\lambda_D \approx R^2/D$. For convenience, we can define Pc for the
 531 initial conditions,

$$Pc = \frac{\lambda_D}{\lambda} = \frac{\Gamma R^2}{D_i \mu_i \langle a_i \rangle} \quad \text{Eq. 7}$$

532

533 where D_i and μ_i are the properties D and μ at the initial H_2O concentration prior to diffusion. If $Pc \ll$
 534 1, then degassing is rapid compared with welding, and $C_i \rightarrow C_e$ early in the welding process. This
 535 manifests as the viscosity moving rapidly from an initial value μ_i determined by C_i , toward a final value
 536 μ_e determined by C_e . However, if $Pc \gg 1$, then welding is rapid compared with degassing, and C_i does
 537 not substantially change during the welding process. This manifests as a near-constant viscosity at μ_i
 538 determined by C_i . Then, in the limiting cases of $Pc \ll 1$ and $Pc \gg 1$, we expect the time at which the
 539 permeability reaches to zero to be approximated by the welding time such that

$$\lambda' = \frac{\mu_e \langle a_i \rangle}{\Gamma} \approx \frac{\mu_e R}{\Gamma} \quad Pc \ll 1 \quad \text{Eq. 8a}$$

$$\lambda' = \frac{\mu_i \langle a_i \rangle}{\Gamma} \approx \frac{\mu_i R}{\Gamma} \quad Pc \gg 1. \quad \text{Eq. 8b}$$

540

541 and for $Pc \sim 1$, we expect that the full model is required to predict the welding time, with no simple
 542 limiting solution available. In Eq. 8 we use the fact that $\langle a_i \rangle$ and R are typically of the same order of
 543 magnitude to make the approximation $\langle a_i \rangle \approx R$, rendering λ' easy to compute in these limiting cases.
 544 In Fig. 9, we plot $\lambda' = \mu_e R / \Gamma$ as the dashed curve (Eq. 8a), and find a minor offset between the limit
 545 that is approached by the solutions and this approximation, which relates to the use of R in place of
 546 $\langle a_i \rangle$. The limit at $Pc \gg 1$ (Eq. 8b) is not a single curve and depends on C_i (Fig. 9).

547 The regime boundary between $Pc \ll 1$ and $Pc \gg 1$ is not necessarily precisely at $Pc = 1$. To test this,
 548 we find the point at which $\lambda = \lambda_D$ for each C_i , which, by definition, is the point at which $Pc = 1$, and
 549 plot this continuously in Fig. 9. The $Pc = 1$ curve cuts the $\lambda'(R)$ curves within their transitional zones
 550 (i.e. the inflected portion) in the majority of cases, indicating that $Pc = 1$ is a reasonable approximation
 551 of the regime boundary. The transitional zone is more sharply defined for high C_i than for low C_i , and
 552 the absolute difference between the low and high Pc solutions is greater for high C_i .

553

554 6.2 Cooling during welding and the preservation of permeable networks

555 In volcanic environments, ignimbrites are emplaced onto a relatively low-temperature substrate, cooling
 556 dynamically during emplacement (Branney and Kokelaar 2002). Similarly, while tuffisites are sourced
 557 in the magmatic conduit itself, they are often emplaced in hydraulic fractures in cold country rock
 558 (Stasiuk et al. 1996). In both cases, dynamic cooling occurs and even simple models show that this can
 559 result in incomplete welding if the material quenches before the welding time is reached (Wadsworth
 560 et al. 2014; Kolzenburg et al. 2019). Indeed, the value that the welding time takes (e.g. Eq. 3; c.f. Eq.
 561 8) is a function of time as the temperature drops.

562 We can apply the approach taken in Section 6.1 for isothermal conditions, to investigate welding
 563 permeability under non-isothermal conditions of continuous cooling. During cooling, the limiting
 564 temperature below which we assume the system is no longer able to weld viscously is the glass
 565 transition temperature T_g . While there is evidence that T_g depends on the cooling rate,– termed q , as

566 $T \rightarrow T_g$ (Gottsmann et al. 2002), we make the simplifying assumption that T_g is the temperature at
 567 which $\mu = 10^{12}$ Pa.s (Gottsmann et al. 2002; Wadsworth et al. 2017a). Using Eq. 3, our full model can
 568 be mapped to any non-isothermal path. However, for simplicity and illustrative purposes, we assume a
 569 linear cooling rate q over the interval between an initial temperature T_i and T_g , which is usually a few
 570 hundred kelvin, and therefore relatively small compared with the total cooling path from T_i to ambient
 571 conditions. During linear cooling, the viscosity of the particles increases and the diffusivity of H₂O
 572 decreases, causing a non-trivial competition between continued degassing of the particles and the
 573 welding rate.

574 In Fig. 10 we show the results of our model runs for non-isothermal environments, which we cast as
 575 the permeability preserved when $T = T_g$. At the fastest cooling rates, little welding occurs before T_g is
 576 reached, and the initial permeability is preserved. At the slowest cooling rates, welding goes to
 577 completion, and permeability drops to zero, by the time T_g is reached. At intermediate cooling rates,
 578 welding is arrested before completion, and the final permeability has a value intermediate between the
 579 initial value and zero. When $C_i = C_e$, hence no degassing occurs, we can see that the final permeability
 580 is a simple, smooth function of q , whereas when $C_i > C_e$, the final permeability may be a more complex
 581 function of q .

582 There is a critical q , which we term q' , below which the permeability will always fall to zero before
 583 $T = T_g$ (Fig. 10). We take q' as a cooling rate of first-order interest, as it separates the regime of
 584 complete welding from the regime of incomplete welding. In Fig. 11 we show the critical q' as a
 585 function of R for the same range of C_i as given for isothermal conditions in Fig. 9. This shows that, for
 586 relatively small particles, the critical cooling rate collapses to a limiting $q'(R)$ for any C_i ; for relatively
 587 large particles, $q'(R)$ evolves toward a second limiting solution at relatively higher q' . Following the
 588 analysis in Section 6.1, we find that the limiting solution $q'(R)$ at small R is the solution for the $Pc \ll$
 589 1. Conversely, the high $q'(R)$ limit at large R is the solution for the $Pc \gg 1$. This implies that there are
 590 again three regimes for a given C_i

- 591 (1) At small R and $q < q'$, welding completes and the resulting deposit is degassed to equilibrium
 592 H₂O concentration.
- 593 (2) At large R and $q < q'$, welding completes but the resulting deposit retains disequilibrium H₂O
 594 concentration.
- 595 (3) At any R and $q > q'$, welding is incomplete, $k > 0$, and t/λ_D can be used to determine if the
 596 deposit is degassed or not, independent of the welding model.

597 In regimes (1) and (2), we can find an analytical solution for the critical cooling rate as

$$q' = \frac{T_i - T_g}{\lambda'} = \frac{(T_i - T_g)\Gamma}{\mu_e \langle a_i \rangle} \approx \frac{(T_i - T_g)\Gamma}{\mu_e R} \quad Pc \ll 1 \quad \text{Eq. 9a}$$

$$q' = \frac{T_i - T_g}{\lambda'} = \frac{(T_i - T_g)\Gamma}{\mu_i \langle a_i \rangle} \approx \frac{(T_i - T_g)\Gamma}{\mu_i R} \quad Pc \gg 1 \quad \text{Eq. 9b}$$

598

599 and as before these regimes are separated by $Pc = 1$ (solid curve on Fig. 11).

600

601 6.3 Direct volcanic applications

602 Welding occurs in volcanic eruptions in distinct scenarios: on the walls of open conduits during Plinian
 603 eruptions (Gardner et al. 2017, 2019); in the hot components of jet engines (Song et al. 2014; Giehl et
 604 al. 2016), in tuffisites (Tuffen and Dingwell 2005; Castro et al. 2012; Heap et al. 2019); at the
 605 depositional base of moving pyroclastic density currents (Branney and Kokelaar 1992, 2002); and

606 during lightning strikes in-air or air-to-ground (Cimarelli et al. 2017; Mueller et al. 2018). While the
607 dynamics of welding is important in controlling the bulk dynamics in all of these scenarios (Wadsworth
608 et al. 2019), we focus on tuffisites and the sedimentation of ignimbrites as the two scenarios where
609 permeability evolution may be most important for understanding outgassing and pressure evolution.
610 Here, we use our model to predict whether a cooling ignimbrite or tuffisite will complete welding before
611 cooling finishes, and whether the final deposit will preserve equilibrium or disequilibrium H₂O.

612 As discussed in Section 6.2, ignimbrites are sedimented onto a substrate that is usually at a lower
613 temperature than the particles deposited; therefore, any initial welding will be strongly non-isothermal
614 and indeed the quench against the substrate may inhibit welding. However, as an ignimbrite
615 accumulates, the cooling rate at any given point may decrease. Depending on the sedimentation rate,
616 the cooling rate may end up being low, especially far from the substrate (Gottsmann and Dingwell
617 2001). Therefore, the average cooling rate from deposition temperature, T_i to T_g , may vary in time and
618 space in welding ignimbrites. By contrast, the particles in tuffisites are emplaced sub-surface and
619 generally involve smaller transport distances; they may therefore be expected to have a higher
620 emplacement temperature compared with ignimbrites. For tuffisites, from a cooling perspective, there
621 are two main types: (1) those that open into hydraulic fractures in viscoelastic magma (Tuffen and
622 Dingwell 2005) and (2) those that open into hydraulic fractures in country rock surrounding the conduit
623 (Stasiuk et al. 1996). In both cases, the expected pressure drop due to fracture propagation may induce
624 adiabatic cooling, but in general, the cooling in case (1) can be expected to be much less than in case
625 (2) (Kolzenburg et al. 2019) and in general a single isothermal temperature is usually estimated when
626 considering the welding dynamics of tuffisites in regime (1) (Castro et al. 2012; Wadsworth et al. 2019;
627 Heap et al. 2019).

628 Any real cooling path will be non-linear and calculation of $T(t)$ requires solution of Fourier's law for
629 conduction. Given that this is geometry and condition dependent, we use a scaling approach, and
630 estimate average cooling rate using $\langle q \rangle \approx (T_i - T_g)D_T/L^2$ where D_T is the thermal diffusivity and L is
631 the system lengthscale in the dominant direction of heat flow. Using data from Bagdassarov and
632 Dingwell (1994) for rhyolitic melts, we can approximate D_T as independent of temperature over the
633 range $700 \leq T \leq 1200$ K and take $D_T = 1 \times 10^{-6}$ m²/s. For ignimbrites, we assume that the lower
634 limit on L is the depositional boundary layer thickness, estimated to be on the order of 1 m (Andrews
635 and Branney 2011) and the upper limit is taken to be 10 m as a reasonable estimate of half-thickness of
636 an entire ignimbrite. For tuffisites, we take the lower limit on L to be 1 mm and the upper limit to be
637 10 cm based on available observations (Castro et al. 2012; Saubin et al. 2016; Heap et al. 2019). In all
638 cases we take T_i to be 1100 K. This results in $10^{-6} \leq \langle q \rangle \leq 10^{-4}$ K.s⁻¹ for ignimbrites, consistent
639 with geospeedometry measurements from glassy welded ignimbrites (Gottsmann and Dingwell 2001),
640 and $10^{-2} \leq \langle q \rangle \leq 10^2$ K.s⁻¹ for tuffisites injected into country rock. For tuffisites injected into
641 viscoelastic magma, the cooling rate will be significantly lower and cooling may not occur. For
642 ignimbrites, while there are clearly larger particles involved (e.g. fiammé), the dominant particle size
643 range is $10^{-5} \leq R \leq 10^{-3}$ m (Branney et al. 1992; Streck and Grunder 1995; Andrews and Branney
644 2011) and a maximum initial H₂O concentration estimate is $C_i = 0.87$ wt.% (Sumner and Branney
645 2002). For tuffisites, the particle size range is similar $10^{-6} \leq R \leq 10^{-3}$ m and $0.7 < C_i < 0.9$ wt.%
646 (Castro et al. 2012; Saubin et al. 2016).

647 In Fig. 12 we use the estimates given above to constrain welding and degassing regimes for tuffisites
648 and ignimbrites, plotting the critical cooling rate q' as a function of radius R of the welding particles
649 (as in Figure 11). Tuffisites plot well above the curves, indicating that they are always expected to
650 quench before they weld under the conditions investigated. This implies that they would remain
651 permeable and potentially act as efficient propped-fractures and outgassing pathways for magmatic
652 gases from the conduit. Ignimbrites can straddle the regimes where welding will or will not occur on
653 the timescale of cooling, consistent with the observation of welded and unwelded ignimbrites in nature.

654 Moreover, for ignimbrites dominated by particles with radius $R \lesssim 2.5 \times 10^{-4}$ m, for which the cooling
 655 is occurring slowly (e.g. fast accumulation rate), our model predicts that the deposit will be degassed
 656 and will weld over the approximate timescale given in Eq. 8b. For ignimbrites dominated by larger
 657 particles $R \gtrsim 2.5 \times 10^{-4}$ m, our model predicts that welding will occur even for high cooling rates
 658 (e.g. slow accumulation rates or basal quenched contacts), but that the deposit will preserve
 659 disequilibrium H₂O concentrations.

660 Both the ignimbrite and tuffisite scenarios investigated in Fig. 12 are in the low- \bar{P} regime, where
 661 confining pressure is small compared with the Laplace surface pressure (Eq. 3). We note that if the
 662 accumulation rate of an ignimbrite is particularly fast, or if the tuffisite is injected at depth, then welding
 663 will instead occur in the high- \bar{P} regime. An increase in \bar{P} moves the $q'(R)$ curves upwards (to faster
 664 cooling rates) compared with their position in Fig. 12. In that regime, welding in ignimbrites is always
 665 expected to occur even under the fastest cooling rates used here, and tuffisites may move into the regime
 666 where welding goes to completion before quench. For example, if we assume that the pressure is
 667 dominantly lithostatic with a mean country rock density of $\rho = 2000 \text{ kg. m}^{-3}$ and the $P_g \approx 2 \text{ MPa}$
 668 described earlier, we can estimate the depth below which even rapidly cooled tuffisites will weld shut
 669 on the timescale of cooling. This depth for a 1 mm tuffisites is 23.2 km and for a 10 cm tuffisite is
 670 475.3 m.

671 Referring back to Fig. 9, isothermal tuffisites injected in hot magma are likely to weld rapidly
 672 (Wadsworth et al. 2019) and to record degassed H₂O contents in the particle fill. This is consistent with
 673 the densely welded nature of tuffisites observed in situ in Icelandic rhyolitic conduits (Tuffen et al.
 674 2003; Tuffen and Dingwell 2005). Tuffisites in obsidian bombs undergo cooling at rates intermediate
 675 between those injected into country rock (Fig. 12) and those welding near-isothermally in conduit
 676 interiors (Fig. 9), and likely cool at rates proportional to the square of the bomb size. The fact that many
 677 bombs preserve tuffisites that are incompletely welded (Heap et al. 2019) suggests that this bomb
 678 cooling rate is greater than q' . However, we note that a model prediction of the end state of permeability
 679 in a bomb would require knowledge of the timing of formation of the tuffisite relative to the time it was
 680 ejected as a bomb, as well as the subsequent cooling path of the bomb – information that at present is
 681 not available for any known example. Nevertheless, our model would predict that these tuffisites span
 682 the range between permeable and impermeable, consistent with observations (Castro et al. 2012; Saubin
 683 et al. 2016; Heap et al. 2019).

684

685 6.4 Outlook: permeability-limited welding and compaction

686 In a welding deposit, there is a competition between the timescale over which welding occurs λ (in the
 687 low- \bar{P} regime), and the timescale over which gas escapes from the welding material λ_0 , which is a
 688 Darcy timescale that depends on the permeability and the length of the system (Michaut et al. 2009;
 689 Wadsworth et al. 2016a; Kennedy et al. 2016; Heap and Wadsworth 2016). If we assume the stress
 690 driving the flow of gas out from between the particles is P_L , then $\lambda_0 = \mu_g L_0^2 \langle a \rangle / (k\Gamma)$ where L_0 is the
 691 distance the gas has to travel to escape the welding system. Using λ_0 we can define a Darcy number as
 692 λ_0 / λ (Wadsworth et al. 2016a)

$$\text{Da} = \frac{\lambda_0}{\lambda} = \frac{\mu_g L_0^2}{k\mu} \quad \text{Eq. 10}$$

693

694 such that at $\text{Da} \ll 1$, outgassing is efficient and welding will complete in the way described by our
 695 model. However for $\text{Da} \gg 1$, the welding is rapid compared with outgassing, and therefore the gas
 696 cannot be driven from the welding system sufficiently quickly, and gas pressure may rise in response
 697 to the Laplace surface pressure that is driving welding. In turn, this can lead to non-linear welding

698 behavior in a regime termed ‘compaction’ by Wadsworth et al. (2019) on the basis that it is expected to
699 be governed by non-linear compaction dynamics described elsewhere (Michaut et al. 2009). While
700 Wadsworth et al. (2019) showed that most volcanic systems are initially in the $Da \ll 1$ regime, our
701 analysis shows that many volcanic systems weld to completion and permeability drops to zero. Since
702 $Da \rightarrow \infty$ as $k \rightarrow 0$ (Eq. 10); it’s clear that $Da \gg 1$ must be met during welding of such systems before
703 welding completes.

704 The implication of Eq. 10 is that, at relatively high porosity in a highly permeable system, the gas phase
705 is truly geochemically open. However, close to the percolation threshold, as the system becomes
706 permeability limited, the gas phase could behave as if it were geochemically closed even in a permeable
707 system. This is qualitatively consistent with the interpretation that the hydrogen-isotope systematics in
708 a range of partially degassed tuffisites show evidence of batched open-closed system behaviour (Castro
709 et al. 2014). This regime remains under-explored.

710

711 7. Using this model: A practical guide

712 We note that the full model presented here is general, such that any pressure–temperature pathway
713 could be incorporated, and the equations solved for $\phi(t)$ and $k(t)$. In this section, we present a short
714 guide for navigating the solutions to our model framework that may be useful in various scenarios of
715 practical interest.

716 To use this model as presented, we provide a VHub resource ‘VolcWeld’ (available at
717 <https://vhub.org/resources/4568>) and a simplified version implemented in Excel™ is provided as
718 Supplementary Material. The full model provided in the ‘VolcWeld’ program solves the full system of
719 equations presented herein and therefore solves for the diffusive movement of H₂O. In turn, this
720 diffusion solution is used to solve the ‘vented bubble model’ for welding and output $\phi(t)$ and $k(t)$.
721 The Excel™ implementation (Supplementary Information), neglects the diffusion of H₂O, and therefore
722 is suited to conditions where H₂O movement can be neglected on the timescale of welding ($Pe \ll 1$ and
723 $Pe \gg 1$; see Section 6), but still solves for the ‘vented bubble model’ using the Euler method for solving
724 ordinary differential equations. The following steps can be followed to determine which solution tool
725 is required:

726 *Initial conditions:*

727 (1) Constrain the particle size distribution $f(R)$ and find the mean particle size $\langle R \rangle$. Both the
728 VolcWeld program and the Excel™ implementation (Supplementary Information) use
729 Wadsworth et al. (2017c) to convert $f(R)$ into a pore size distribution $f(a_i)$ and find the mean
730 pore size $\langle a_i \rangle$. If no information about the full distribution of particle sizes is known, then take
731 an estimate for the typical particle size and define this as $\langle R \rangle$.

732

733 (2) Measure the initial H₂O concentration of the particles and determine whether or not this is in
734 equilibrium by calculating the H₂O solubility using a constitutive law (e.g. Liu et al. 2005).
735 Estimate the gas and liquid pressures and initial temperature of the system.

736 *Isothermal welding*

737 (3) If the system is in H₂O equilibrium and is isothermal, then no diffusion will occur and our
738 Excel™ implementation can be used (Supplementary Information). In this situation, for scaling
739 purposes, one can compute the melt viscosity μ_i (e.g. Hess and Dingwell 1996), use $\Gamma =$
740 $0.3 \text{ N} \cdot \text{m}^{-1}$, and use $\langle a_i \rangle$ from step (1) to compute a welding timescale.

741

- 742 (4) If the system is not in H₂O equilibrium (see step (2)), then calculate the H₂O diffusivity D_i (e.g.
743 Zhang and Ni 2010) and melt viscosity μ_i (e.g. Hess and Dingwell 1996) under initial
744 conditions. Using $\Gamma = 0.3 \text{ N} \cdot \text{m}^{-1}$, calculate the capillary Peclet number $\text{Pc} = \Gamma R^2 / (D_i \mu_i \langle a_i \rangle)$
745 for these initial conditions. If $\text{Pc} \leq 0.1$ or $\text{Pc} \geq 10$, use the initial or equilibrium H₂O
746 concentration to compute the melt viscosity, respectively. In either case, our Excel™
747 implementation can be used (Supplementary Information). If instead $0.1 > \text{Pc} < 10$, then the
748 diffusive movement of H₂O renders the problem more complex and the VolcWeld program can
749 be used (available at Vhub).

750
751 *For non-isothermal cooling conditions:*

- 752
753 (5) As with isothermal conditions, the Excel™ implementation can be used for $\text{Pc} \leq 0.1$ or $\text{Pc} \geq$
754 10 , where the first sheet in the implementation permits input of a temperature rate q . If,
755 however, $0.1 > \text{Pc} < 10$, then the VolcWeld program must be used.

756 757 **8. Summary and conclusions**

758 We have experimentally validated a mathematical model that can predict how the Darcian permeability
759 of welding deposits evolves with time, including the effect of syn-welding volatile diffusion and non-
760 isothermal cooling paths, which are typical of natural scenarios. We use our new experimental and
761 simulation data for the permeability of welded obsidian particles collected *in situ* to validate our model
762 across a range of temperatures. We take an additional validation step by comparing the component parts
763 of our model to natural and experimental data for other compositions, temperatures, particle sizes, and
764 conditions, and conclude that our model is generally applicable for small systems. Across all isothermal
765 conditions, we identify three dynamic regimes captured by the capillary Peclet number, (1) at $\text{Pc} \ll 1$,
766 deposits degas rapidly and weld to preserve equilibrium low H₂O concentration, (2) at $\text{Pc} \gg 1$, deposits
767 weld rapidly to preserve high near-initial disequilibrium H₂O concentration, and (3) at intermediate
768 $\text{Pc} = 1$, welding produces partially degassed deposits. In cooling systems, we find the additional effect
769 that deposits may cool before they weld or degas, preserving permeable systems that did not completely
770 seal.

771 We show that, for all reasonable conditions, tuffisites injected in colder country rock are likely to
772 quench before welding, preserving permeable pathways. By contrast, we show that ignimbrites straddle
773 the critical cooling rates below which welding can complete and above which it cannot, suggesting that
774 the details of the emplacement temperature, cooling rates, particle radii, and initial H₂O concentration
775 are critical controls on whether an ignimbrite will be welded or not. This same approach shows that if
776 ignimbrites are welded, then whether or not they are fully degassed depends primarily on the particle
777 size. We anticipate that the model framework that we develop will find application in studies of the
778 dynamics of outgassing, and implications for eruptive processes.

779

780

781

782 **Acknowledgments**

783 We thank Holly Unwin for useful input in the field in the summer of 2019, and Mathieu Colombier,
784 Sebastian Wiesmaier, and Julie Fife for beamtime support. We acknowledge the Paul Scherrer Institut,
785 Villigen, Switzerland for provision of synchrotron radiation beamtime at the TOMCAT beamline of the
786 SLS. Funding was provided by the European Research Council (Advanced Grant EAVESDROP
787 834225; Starting Grant SLiM 306488), the Natural Environment Research Council grants
788 (NE/N002954/1, NE/M018687/1, and NE/M018687/2), and the National Science Foundation (NSF
789 EAR-1852449). All raw data associated with the experiments presented herein (c.f. Figures 4-6) and
790 required to reproduce our analysis is available in the Supplementary Information. We are grateful to
791 Kelly Russell for editorial oversight and to two reviewers for careful comments on our work which led
792 to improvements.

793

794 **Author contributions**

795 Wadsworth, Vasseur and Llewellyn derived the mathematical model and led the data analysis. Vasseur
796 and Wadsworth developed the online resource VolcWeld, which is used and updated herein (Vasseur
797 and Wadsworth 2019). Brown, Tuffen, and Gardner provided context and images from welded deposits.
798 Schaubroth and Dobson led the Avizo™ segmentation work. Wadsworth, von Aulock, Dobson,
799 Schaubroth, and Vasseur assisted at the beamline. Lavallée, Dingwell, and Hess provided laboratory,
800 logistical and financial support. Kendrick, Heap, and Kushnir, contributed additional data and context
801 for application of the model. Marone is the beamline scientist supporting this work. All authors
802 contributed to the manuscript.

803

804 **References cited**

- 805 Almond DC (1971) Ignimbrite vents in the Sabaloka cauldron, Sudan. *Geol Mag* 108:159–176.
806 <https://doi.org/10.1017/S0016756800051190>
- 807 Andrews GDM, Branney MJ (2011) Emplacement and rheomorphic deformation of a large, lava-like
808 rhyolitic ignimbrite: Grey's Landing, southern Idaho. *Geol Soc Am Bull* 123:725–743.
809 <https://doi.org/10.1130/b30167.1>
- 810 Bagdassarov N, Dingwell D (1994) Thermal properties of vesicular rhyolite. *J Volcanol Geotherm*
811 *Res* 60:179–191
- 812 Berlo K, Tuffen H, Smith VC, et al (2013) Element variations in rhyolitic magma resulting from gas
813 transport. *Geochim Cosmochim Acta* 121:436–451
- 814 Blair SC, Berge PA, Berryman JG (1993) Two-point correlation functions to characterize
815 microgeometry and estimate permeabilities of synthetic and natural sandstones. Lawrence
816 Livermore National Lab., CA (United States)
- 817 Branney MJ, Kokelaar BP (2002) Pyroclastic density currents and the sedimentation of ignimbrites.
818 The Geological Society of London, London
- 819 Branney MJ, Kokelaar BpP, McConnell B (1992) The Bad Step Tuff: a lava-like rheomorphic
820 ignimbrite in a calc-alkaline piecemeal caldera, English Lake District. *Bull Volcanol* 54:187–
821 199. <https://doi.org/10.1007/BF00278388>
- 822 Branney MJ, Kokelaar P (1992) A reappraisal of ignimbrite emplacement: progressive aggradation
823 and changes from particulate to non-particulate flow during emplacement of high-grade
824 ignimbrite. *Bull Volcanol* 54:504–520. <https://doi.org/10.1007/BF00301396>

- 825 Casas AS, Wadsworth FB, Ayris PM, et al (2019) SO₂ scrubbing during percolation through rhyolitic
826 volcanic domes. *Geochim Cosmochim Acta*. <https://doi.org/10.1016/j.gca.2019.04.013>
- 827 Castro JM, Bindeman IN, Tuffen H, Ian Schipper C (2014) Explosive origin of silicic lava: Textural
828 and $\delta\text{D-H}_2\text{O}$ evidence for pyroclastic degassing during rhyolite effusion. *Earth Planet Sci Lett*
829 405:52–61. <https://doi.org/10.1016/j.epsl.2014.08.012>
- 830 Castro JM, Cordonnier B, Tuffen H, et al (2012) The role of melt-fracture degassing in defusing
831 explosive rhyolite eruptions at volcán Chaitén. *Earth Planet Sci Lett* 333:63–69.
832 <https://doi.org/http://dx.doi.org/10.1016/j.epsl.2012.04.024>
- 833 Cimarelli C, Yilmaz T, Colombier M, et al (2017) Micro-and nano-CT textural analysis of an
834 experimental volcanic fulgurite. *EGU Gen Assem Conf Abstr* 19:17982
- 835 Colombier M, Wadsworth FFB, Gurioli L, et al (2017) The evolution of pore connectivity in volcanic
836 rocks. 462:. <https://doi.org/10.1016/j.epsl.2017.01.011>
- 837 Crank J (1975) The mathematics of diffusion
- 838 Eichheimer P, Thielmann M, Fujita W, et al (2020) Combined numerical and experimental study of
839 microstructure and permeability in porous granular media. *Solid Earth* 11:1079–1095.
840 <https://doi.org/10.5194/se-11-1079-2020>
- 841 Elam WT, Kerstein AR, Rehr JJ (1984) Critical properties of the void percolation problem for
842 spheres. *Phys Rev Lett* 52:1516
- 843 Farquharson JI, Wadsworth FB, Heap MJ, Baud P (2017) Time-dependent permeability evolution in
844 compacting volcanic fracture systems and implications for gas overpressure. *J Volcanol*
845 *Geotherm Res* 339:81–97. <https://doi.org/10.1016/j.jvolgeores.2017.04.025>
- 846 Feng S, Halperin BBI, Sen PPN (1987) Transport properties of continuum systems near the
847 percolation threshold. *Phys Rev B* 35:197
- 848 Fife JL, Rappaz M, Pistone M, et al (2012) Development of a laser-based heating system for in situ
849 synchrotron-based X-ray tomographic microscopy. *J Synchrotron Radiat* 19:352–358
- 850 Gardner JE, Llewellyn EW, Watkins JM, Befus KS (2017) Formation of obsidian pyroclasts by
851 sintering of ash particles in the volcanic conduit. *Earth Planet Sci Lett* 459:252–263.
852 <https://doi.org/10.1016/J.EPSL.2016.11.037>
- 853 Gardner JE, Wadsworth FB, Llewellyn EW, et al (2018) Experimental sintering of ash at conduit
854 conditions and implications for the longevity of tuffisites. *Bull Volcanol* 80:23.
855 <https://doi.org/10.1007/s00445-018-1202-8>
- 856 Gardner JE, Wadsworth FB, Llewellyn EW, et al (2019) Experimental constraints on the textures and
857 origin of obsidian pyroclasts. *Bull Volcanol* 81:22. <https://doi.org/10.1007/s00445-019-1283-z>
- 858 Giehl C, Brooker R, Marxer H, Nowak M (2016) An experimental simulation of volcanic ash
859 deposition in gas turbines and implications for jet engine safety. *Chem Geol*
- 860 Gottsmann J, Dingwell DB (2001) Cooling dynamics of spatter-fed phonolite obsidian flows on
861 Tenerife, Canary Islands. *J Volcanol Geotherm Res* 105:323–342.
862 [https://doi.org/10.1016/S0377-0273\(00\)00262-6](https://doi.org/10.1016/S0377-0273(00)00262-6)
- 863 Gottsmann J, Giordano D, Dingwell DB (2002) Predicting shear viscosity during volcanic processes
864 at the glass transition: a calorimetric calibration. *Earth Planet Sci Lett* 198:417–427
- 865 Harris PD, Branney MJ, Storey M (2011) Large eruption-triggered ocean-island landslide at Tenerife:
866 Onshore record and long-term effects on hazardous pyroclastic dispersal. *Geology* 39:951–954.
867 <https://doi.org/10.1130/G31994.1>

- 868 Heap MJ, Farquharson JJ, Wadsworth FB, et al (2015) Timescales for permeability reduction and
869 strength recovery in densifying magma. *Earth Planet Sci Lett* 429:223–233.
870 <https://doi.org/10.1016/j.epsl.2015.07.053>
- 871 Heap MJ, Gilg HA, Byrne PK, et al (2020) Petrophysical properties, mechanical behaviour, and
872 failure modes of impact melt-bearing breccia (suevite) from the Ries impact crater (Germany).
873 *Icarus* 349:113873. <https://doi.org/10.1016/j.icarus.2020.113873>
- 874 Heap MJ, Kolzenburg S, Russell JK, et al (2014) Conditions and timescales for welding block-and-
875 ash flow deposits. *J Volcanol Geotherm Res* 289:202–209.
876 <https://doi.org/10.1016/j.jvolgeores.2014.11.010>
- 877 Heap MJ, Tuffen H, Wadsworth FB, et al (2019) The Permeability Evolution of Tuffisites and
878 Implications for Outgassing Through Dense Rhyolitic Magma. *J Geophys Res Solid Earth*
879 124:8281–8299. <https://doi.org/10.1029/2018jb017035>
- 880 Heap MJ, Wadsworth FB (2016) Closing an open system: Pore pressure changes in permeable edifice
881 rock at high strain rates. *J Volcanol Geotherm Res* 315:40–50.
882 <https://doi.org/10.1016/j.jvolgeores.2016.02.011>
- 883 Heiken G, Wohletz K, Eichelberger J (1988) Fracture fillings and intrusive pyroclasts, Inyo Domes,
884 California. *J Geophys Res* 93:4335–4350. <https://doi.org/10.1029/JB093iB05p04335>
- 885 Hess KU, Dingwell DB (1996) Viscosities of hydrous leucogranitic melts: A non-Arrhenian model.
886 *Am Mineral* 81:1297–1300
- 887 Houghton B, Carey RJ (2015) Pyroclastic Fall Deposits. In: *The Encyclopedia of Volcanoes*. pp 599–
888 616
- 889 Kendrick JE, Lavallée Y, Varley NR, et al (2016) Blowing off steam: Tuffisite formation as a
890 regulator for lava dome eruptions. *Front Earth Sci* 4:41. <https://doi.org/10.3389/feart.2016.00041>
- 891 Kennedy BM, Wadsworth FB, Vasseur J, et al (2016) Surface tension driven processes densify and
892 retain permeability in magma and lava. *Earth Planet Sci Lett* 433:116–124.
893 <https://doi.org/10.1016/j.epsl.2015.10.031>
- 894 Kertész J (1981) Percolation of holes between overlapping spheres: Monte Carlo calculation of the
895 critical volume fraction. *J Phys Lettres* 42:393–395
- 896 Kolzenburg S, Heap MJ, Lavallée Y, et al (2012) Strength and permeability recovery of tuffisite-
897 bearing andesite. *Solid Earth* 3:191–198. <https://doi.org/10.5194/se-3-191-2012>
- 898 Kolzenburg S, Ryan AG, Russell JK (2019) Permeability evolution during non-isothermal
899 compaction in volcanic conduits and tuffisite veins: Implications for pressure monitoring of
900 volcanic edifices. *Earth Planet Sci Lett* 527:115783. <https://doi.org/10.1016/j.epsl.2019.115783>
- 901 Lange RA, Carmichael ISE (1987) Densities of Na₂O-K₂O-MgO-MgO-FeO-Fe₂O₃-Al₂O₃-TiO₂-
902 SiO₂ liquids: New measurements and derived partial molar properties. *Geochim Cosmochim*
903 *Acta* 51:2931–2946
- 904 Lavallée Y, Wadsworth FB, Vasseur JJ, et al (2015) Eruption and emplacement timescales of
905 ignimbrite super-eruptions from thermo-kinetics of glass shards. *Front Earth Sci* 3:2.
906 <https://doi.org/10.3389/feart.2015.00002>
- 907 Lewiner T, Lopes H, Vieira AAW, Tavares G (2003) Efficient implementation of marching cubes'
908 cases with topological guarantees. 8:1–15
- 909 Liu Y, Zhang Y, Behrens H (2005) Solubility of H₂O in rhyolitic melts at low
910 pressures and a new empirical model for mixed H₂O–CO₂ solubility in rhyolitic melts. *J Volcanol Geotherm Res* 143:219–235
911

- 912 Llewellyn EW (2010a) LBflow: An extensible lattice Boltzmann framework for the simulation of
913 geophysical flows. Part II: usage and validation. *Comput Geosci* 36:123–132.
914 <https://doi.org/10.1016/j.cageo.2009.08.003>
- 915 Llewellyn EW (2010b) LBflow: An extensible lattice Boltzmann framework for the simulation of
916 geophysical flows. Part I: theory and implementation. *Comput Geosci* 36:115–122.
917 <https://doi.org/10.1016/j.cageo.2009.08.004>
- 918 Lorensen W, Cline H (1987) Marching cubes: A high resolution 3D surface construction algorithm.
919 *ACM siggraph Comput Graph*
- 920 Mackenzie JK, Shuttleworth R (1949) A phenomenological theory of sintering. *Proc Phys Soc Sect B*
921 62:833
- 922 Martys NS, Torquato S, Bentz DP (1994) Universal scaling of fluid permeability for sphere packings.
923 *Phys Rev E* 50:403
- 924 Michaut C, Bercovici D, Sparks RSJ (2009) Ascent and compaction of gas rich magma and the effects
925 of hysteretic permeability. *Earth Planet Sci Lett* 282:258–267
- 926 Mueller S, Melnik O, Spieler O, et al (2005) Permeability and degassing of dome lavas undergoing
927 rapid decompression: An experimental determination. *Bull Volcanol* 67:526–538
- 928 Mueller SP, Helo C, Keller F, et al (2018) First experimental observations on melting and chemical
929 modification of volcanic ash during lightning interaction. *Sci Rep* 8:1389.
930 <https://doi.org/10.1038/s41598-018-19608-3>
- 931 Okumura S, Sasaki O (2014) Permeability reduction of fractured rhyolite in volcanic conduits and its
932 control on eruption cyclicity. *Geology* 42:843–846
- 933 Owen J, Shea T, Tuffen H (2019) Basalt, Unveiling Fluid-filled Fractures, Inducing Sediment Intra-
934 void Transport, Ephemeral: Examples from Katla 1918. *J Volcanol Geotherm Res* 369:121–
935 144. <https://doi.org/10.1016/j.jvolgeores.2018.11.002>
- 936 Paisley R, Berlo K, Whattam J, et al (2019) Degassing-induced chemical heterogeneity at the 2011-
937 2012 Cordón Caulle eruption. *Volcanica* 2:211–237. <https://doi.org/10.30909/vol.02.02.211237>
- 938 Parikh NM (1958) Effect of atmosphere on surface tension of glass. *J Am Ceram Soc* 41:18–22
- 939 Prado M, Dutra Zanotto E, Müller R (2001) Model for sintering polydispersed glass particles. *J Non*
940 *Cryst Solids* 279:169–178
- 941 Quane SL, Russell JK (2005a) Welding: insights from high-temperature analogue experiments. *J*
942 *Volcanol Geotherm Res* 142:67–87.
943 <https://doi.org/http://dx.doi.org/10.1016/j.jvolgeores.2004.10.014>
- 944 Quane SL, Russell JK (2005b) Ranking welding intensity in pyroclastic deposits. *Bull Volcanol*
945 67:129–143
- 946 Quane SL, Russell JK, Friedlander EA (2009) Time scales of compaction in volcanic systems.
947 *Geology* 37:471–474
- 948 Rahaman MN, De Jonghe LC (1990) Sintering of Spherical Glass Powder under a Uniaxial Stress. *J*
949 *Am Ceram Soc* 73:707–712. <https://doi.org/10.1111/j.1151-2916.1990.tb06576.x>
- 950 Riehle JR (1973) Calculated Compaction Profiles of Rhyolitic Ash-Flow Tuffs. *Bull Geol Soc Am*
951 84:2193–2216. [https://doi.org/10.1130/0016-7606\(1973\)84<2193:CCPORA>2.0.CO;2](https://doi.org/10.1130/0016-7606(1973)84<2193:CCPORA>2.0.CO;2)
- 952 Riehle JR, Miller TF, Bailey RA (1995) Cooling, degassing and compaction of rhyolitic ash flow
953 tuffs: a computational model. *Bull Volcanol* 57:319–336. <https://doi.org/10.1007/BF00301291>
- 954 Russell JK, Quane SL (2005) Rheology of welding: inversion of field constraints. *J Volcanol*

955 Geotherm Res 142:173–191. <https://doi.org/http://dx.doi.org/10.1016/j.jvolgeores.2004.10.017>

956 Ryan AG, Friedlander EA, Russell JK, et al (2018) Hot pressing in conduit faults during lava dome
957 extrusion: Insights from Mount St. Helens 2004–2008. *Earth Planet Sci Lett* 482:171–180.
958 <https://doi.org/10.1016/j.epsl.2017.11.010>

959 Ryan AG, Heap MJ, Russell JK, et al (2020a) Cyclic shear zone cataclasis and sintering during lava
960 dome extrusion: Insights from Chaos Crags, Lassen Volcanic Center (USA). *J Volcanol*
961 *Geotherm Res* 401:106935. <https://doi.org/10.1016/j.jvolgeores.2020.106935>

962 Ryan AG, Russell JK, Heap MJ, et al (2020b) Timescales of porosity and permeability loss by solid-
963 state sintering. *Earth Planet Sci Lett* 549:116533. <https://doi.org/10.1016/j.epsl.2020.116533>

964 Sánchez MC, Sarrionandia F, Arostegui J, et al (2012) The transition of spatter to lava-like body in
965 lava fountain deposits: features and examples from the Cabezo Segura volcano (Calatrava,
966 Spain). *J Volcanol Geotherm Res*

967 Saubin E, Tuffen H, Gurioli L, et al (2016) Conduit Dynamics in Transitional Rhyolitic Activity
968 Recorded by Tuffisite Vein Textures from the 2008–2009 Chaitén Eruption. *Front Earth Sci* 4:.
969 <https://doi.org/10.3389/feart.2016.00059>

970 Schipper CI, Castro JM, Tuffen H, et al (2015) Cristobalite in the 2011–2012 Cordon Caulle eruption
971 (Chile). *Bull Volcanol* 77:.. <https://doi.org/10.1007/s00445-015-0925-z>

972 Song W, Hess KK-U, Damby DEDE, et al (2014) Fusion characteristics of volcanic ash relevant to
973 aviation hazards. *Geophys Res Lett* 41:2326–2333. <https://doi.org/10.1002/2013GL059182>

974 Sparks RSJ, Tait SR, Yanev Y (1999) Dense welding caused by volatile resorption. *J Geol Soc*
975 London 156:217–225. <https://doi.org/10.1144/gsjgs.156.2.0217>

976 Stasiuk M V, Barclay J, Carroll MR, et al (1996) Degassing during magma ascent in the Mule Creek
977 vent (USA). *Bull Volcanol* 58:117–130

978 Streck MJ, Grunder AL (1995) Crystallization and welding variations in a widespread ignimbrite
979 sheet; the Rattlesnake Tuff, eastern Oregon, USA. *Bull Volcanol* 57:151–169

980 Sumner JM, Blake S, Matela RJ, Wolff JA (2005) Spatter. *J Volcanol Geotherm Res* 142:49–65

981 Sumner JM, Branney MJ (2002) The emplacement history of a remarkable heterogeneous, chemically
982 zoned, rheomorphic and locally lava-like ignimbrite: ‘TL’ on Gran Canaria. *J Volcanol*
983 *Geotherm Res* 115:109–138. [https://doi.org/10.1016/S0377-0273\(01\)00311-0](https://doi.org/10.1016/S0377-0273(01)00311-0)

984 Torquato S (2013) Random heterogeneous materials: microstructure and macroscopic properties.
985 Springer Science & Business Media

986 Tuffen H, Dingwell D (2005) Fault textures in volcanic conduits: evidence for seismic trigger
987 mechanisms during silicic eruptions. *Bull Volcanol* 67:370–387. <https://doi.org/10.1007/s00445-004-0383-5>

988

989 Tuffen H, Dingwell DB, Pinkerton H (2003) Repeated fracture and healing of silicic magma generate
990 flow banding and earthquakes? *Geology* 31:1089–1092. <https://doi.org/10.1130/g19777.1>

991 Vasseur J, Wadsworth F (2019) Volcanic welding model: VolcWeld. <https://vhub.org/resources/4568>.
992 Accessed 9 Jul 2019

993 Vasseur J, Wadsworth FB (2017) Sphere models for pore geometry and fluid permeability in
994 heterogeneous magmas. *Bull Volcanol* 79:77. <https://doi.org/10.1007/s00445-017-1165-1>

995 Vasseur J, Wadsworth FB, Dingwell DB (2020) Permeability of polydisperse magma foam. *Geology*.
996 <https://doi.org/10.1130/G47094.1>

997 Vasseur J, Wadsworth FB, Lavallée Y, et al (2013) Volcanic sintering: Timescales of viscous

998 densification and strength recovery. *Geophys Res Lett* 40:5658–5664.
999 <https://doi.org/10.1002/2013GL058105>

1000 Von Aulock FW, Kennedy BM, Maksimenko A, et al (2017) Outgassing from open and closed
1001 magma foams. *Front Earth Sci* 5:. <https://doi.org/10.3389/feart.2017.00046>

1002 Wadsworth FB, Llewellyn EW, Vasseur J, et al (2020a) Explosive–effusive volcanic eruption
1003 transitions caused by sintering. *Sci Adv* 6:7940–7963. <https://doi.org/10.1126/sciadv.aba7940>

1004 Wadsworth FB, Vasseur J, Aulock FW, et al (2014) Nonisothermal viscous sintering of volcanic ash.
1005 *J Geophys Res Solid Earth* 119:8792–8804. <https://doi.org/10.1002/2014JB011453>

1006 Wadsworth FB, Vasseur J, Llewellyn EW, et al (2016a) Sintering of viscous droplets under surface
1007 tension. *Proc R Soc A Math Phys Eng Sci* 472:20150780.
1008 <https://doi.org/10.1098/rspa.2015.0780>

1009 Wadsworth FB, Vasseur J, Llewellyn EW, et al (2017a) Size limits for rounding of volcanic ash
1010 particles heated by lightning. *J Geophys Res Solid Earth* 122:1977–1989.
1011 <https://doi.org/10.1002/2016JB013864>

1012 Wadsworth FB, Vasseur J, Llewellyn EW, et al (2017b) Topological inversions in coalescing granular
1013 media control fluid-flow regimes. *Phys Rev E* 96:033113.
1014 <https://doi.org/10.1103/PhysRevE.96.033113>

1015 Wadsworth FB, Vasseur J, Llewellyn EW, Dingwell DB (2017c) Sintering of polydisperse viscous
1016 droplets. *Phys Rev E* 95:. <https://doi.org/10.1103/PhysRevE.95.033114>

1017 Wadsworth FB, Vasseur J, Llewellyn EW, Dingwell DB (2017d) Sintering of polydisperse viscous
1018 droplets. *Phys Rev E* 95:033114. <https://doi.org/10.1103/PhysRevE.95.033114>

1019 Wadsworth FB, Vasseur J, Schaubert J, et al (2019) A general model for welding of ash particles in
1020 volcanic systems validated using in situ X-ray tomography. *Earth Planet Sci Lett* 525:115726.
1021 <https://doi.org/10.1016/j.epsl.2019.115726>

1022 Wadsworth FB, Vasseur J, Scheu B, et al (2016b) Universal scaling of fluid permeability during
1023 volcanic welding and sediment diagenesis. *Geology* 44:219–222.
1024 <https://doi.org/10.1130/G37559.1>

1025 Wadsworth FB, Vossen CEJ, Schmid D, et al (2020b) Determination of permeability using a classic
1026 Darcy water column. *Am J Phys* 88:20–24. <https://doi.org/10.1119/10.0000296>

1027 Wright HM, Cashman K V (2014) Compaction and gas loss in welded pyroclastic deposits as
1028 revealed by porosity, permeability, and electrical conductivity measurements of the Shevlin Park
1029 Tuff. *Geol Soc Am Bull* 126:234–247. <https://doi.org/10.1130/b30668.1>

1030 Zhang Y, Ni H (2010) Diffusion of H, C, and O components in silicate melts. *Rev Mineral*
1031 *Geochemistry* 72:171–225

1032

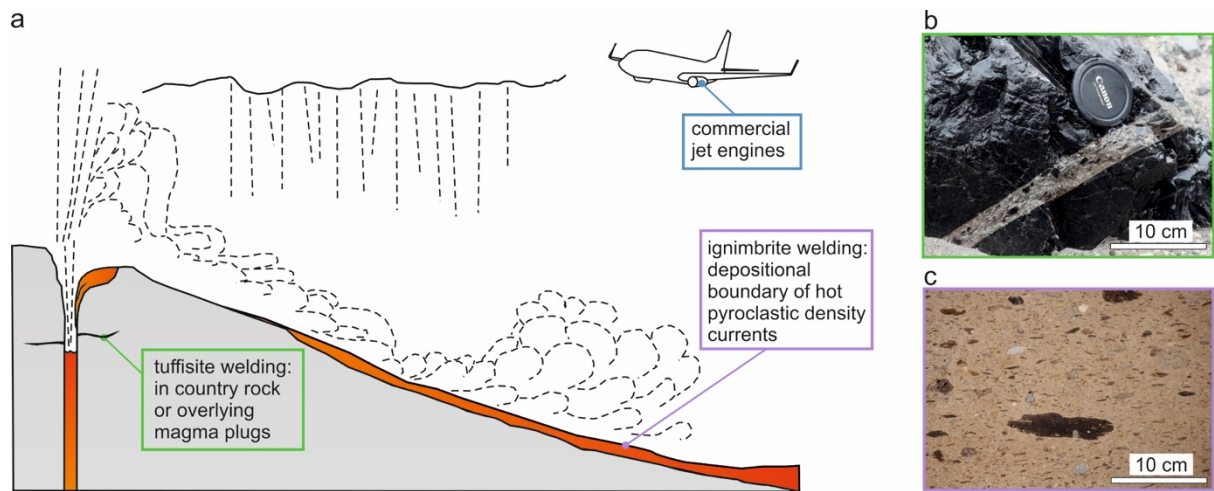
1033

1034 Table 1 – in separate file.

1035

1036

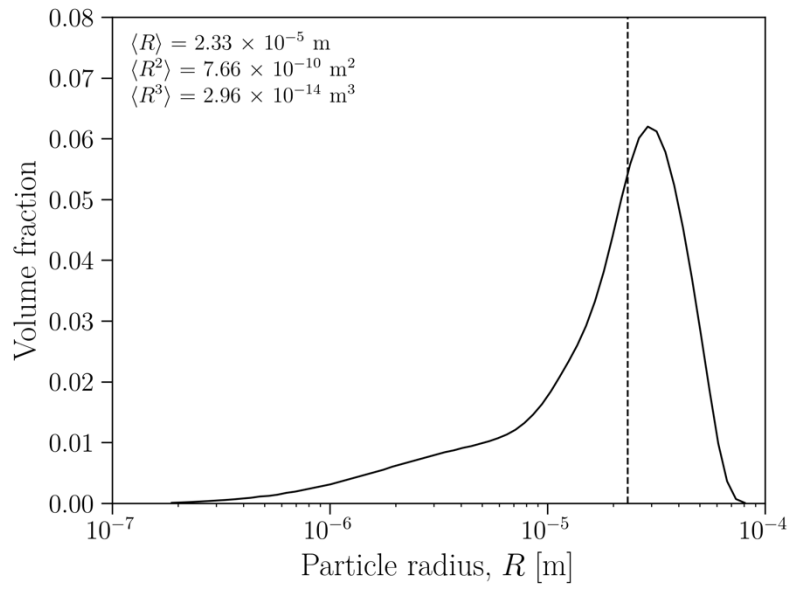
1037
1038
1039
1040



1041

1042 **Figure 1.** Settings in which welding of volcanic particles occurs. (a) A schematic of a generic explosive
1043 eruption (re-drawn and adapted from Harris et al. 2011). Welding may occur in tuffisites (black veins)
1044 which hydraulically fracture country rock or overlying magma, in the deposits of pyroclastic density
1045 currents on the volcano flanks, and in aircraft jet engines. Here, we focus on tuffisites and ignimbrites.
1046 (b) A tuffisite hosted in obsidian from the 2008 eruption of Volcán Chaiten (image from Heap et al.
1047 2019). (c) Detail of a partially welded ignimbrite from the 668 ka phonolitic Arico eruption of Las
1048 Cañadas volcano, Tenerife (image courtesy of Rich Brown).

1049

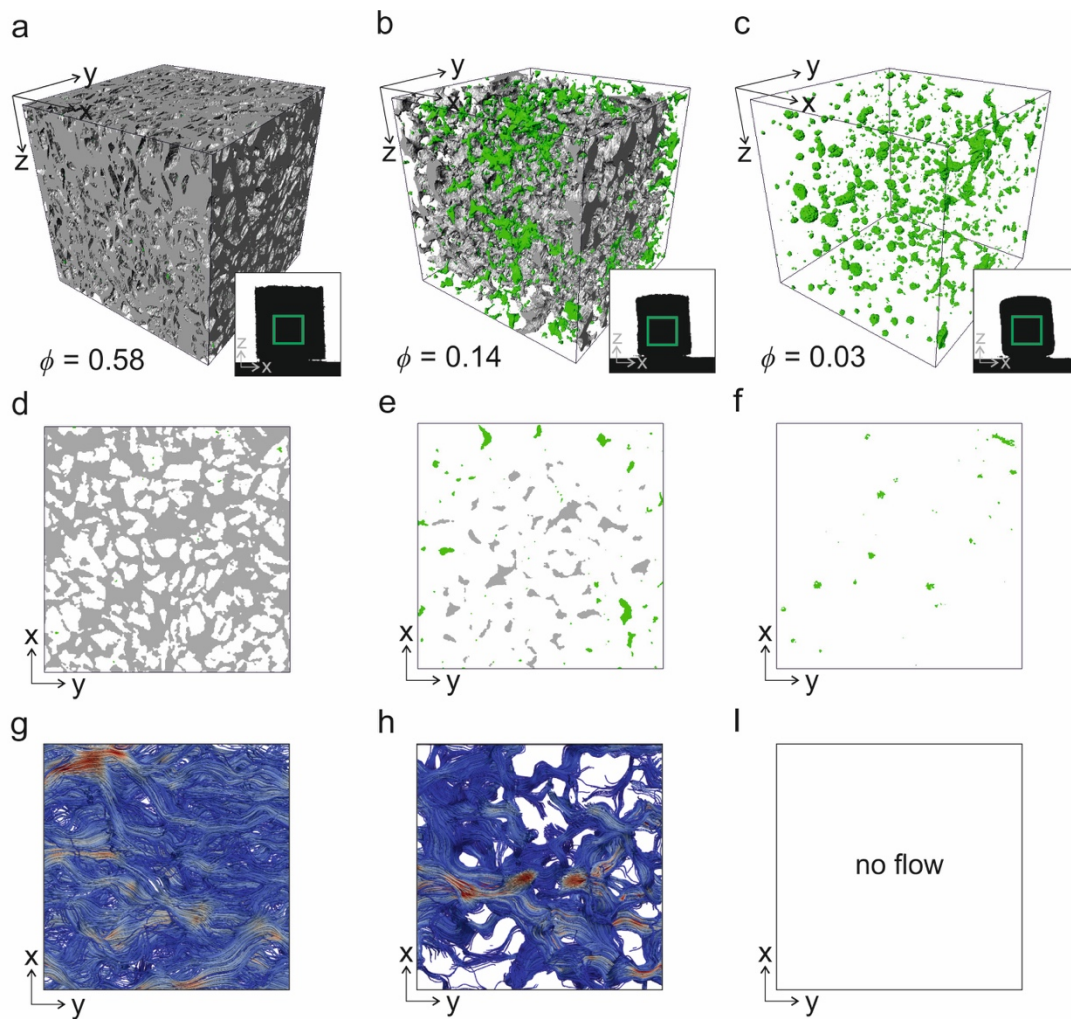


1050

1051 **Figure 2.** The particle size distribution used in the experiments presented in Wadsworth et al. (2019)
1052 and re-analyzed herein. The values for the first, second, and third moments of the distribution are given
1053 on the figure and the first moment (mean) is indicated with a vertical dashed line. The data are binned
1054 at 0.04 log units in R .

1055

1056

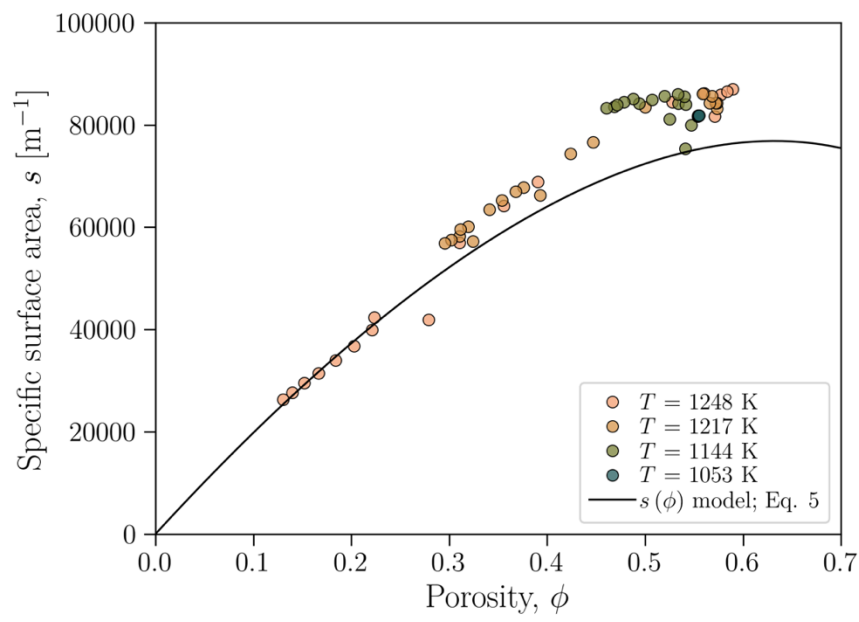


1058

1059 **Figure 3.** Internal textures in packs of volcanic particles that are welding at high temperature, imaged
 1060 using *in situ* x-ray tomography. (a-c) 3D renderings of the pore spaces using grey to denote pores that
 1061 are connected from edge-to-edge and green to denote pores that are isolated from through-going
 1062 connections (*Insets*: the full exterior sample shape in 2D showing the evolution of relative 2D area of
 1063 the side of the free-standing cylinders). (d-f) 2D slices of the same sample time-steps given in (a-c). (g-
 1064 i) Collapsed 2D views of the steady-state fluid flow vector distribution computed using LBflow and
 1065 visualized using Paraview. Red and blue colours respectively indicate relatively high and low flow
 1066 speeds; the absolute values of the colour scale are arbitrary and for comparison only.

1067

1068

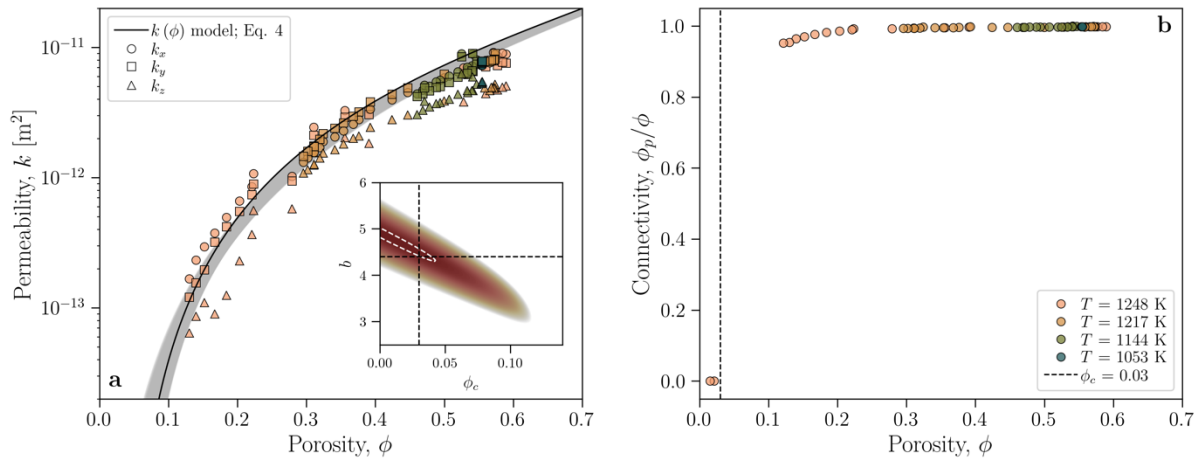


1069

1070 **Figure 4.** The relationship between specific surface area s and porosity ϕ during high-temperature
1071 welding of a pack of volcanic particles. Both s and ϕ are determined from analysis of tomographic data
1072 (Section 3.1).

1073

1074



1075

1076 **Figure 5.** The relationship between porosity ϕ and permeability k of welding systems. (a) The $k(\phi)$
 1077 data for the *in situ* experiments analyzed here. The solution to the $k(\phi)$ model using Eq. 4 is shown for
 1078 $\phi_c = 0.03$ and $b = 4.4$ (Feng et al. 1987). The grey band represents the range of model solutions that
 1079 encompass 2% uncertainty around the best fit ϕ_c and b pair. *Inset:* the goodness of fit (fit in logarithmic
 1080 space) given by a Deming r^2 (see text) of Eq. 4 for different ϕ_c and b value pairs, for which the best-
 1081 fit value is indicated with the dashed line. The region of ϕ_c and b value pairs given by the grey band
 1082 in (a) is enclosed by the white dashed line. (b) The relationship between the pore connectivity ϕ_p/ϕ
 1083 and ϕ .

1084

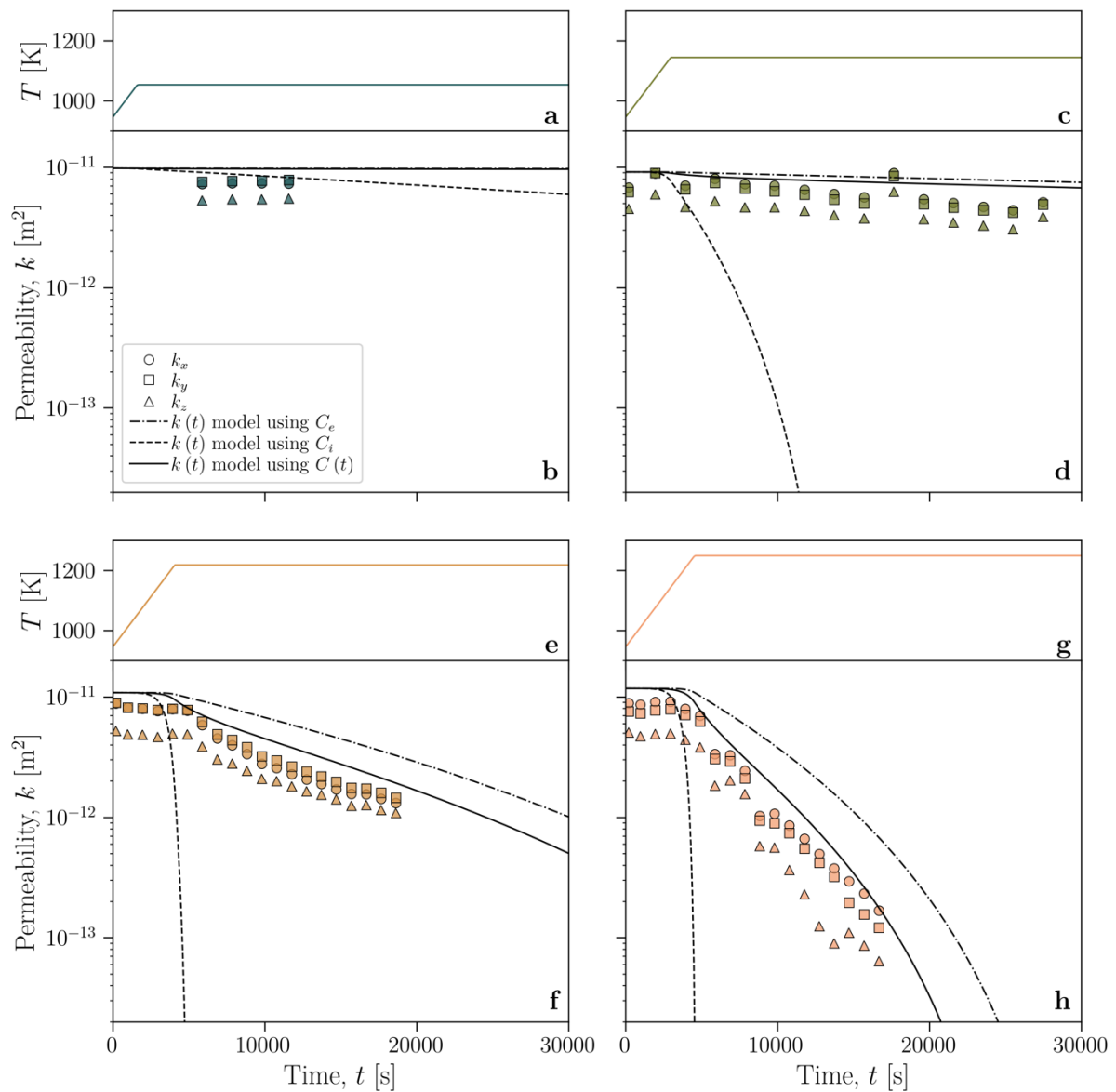
1085

1086

1087

1088

1089

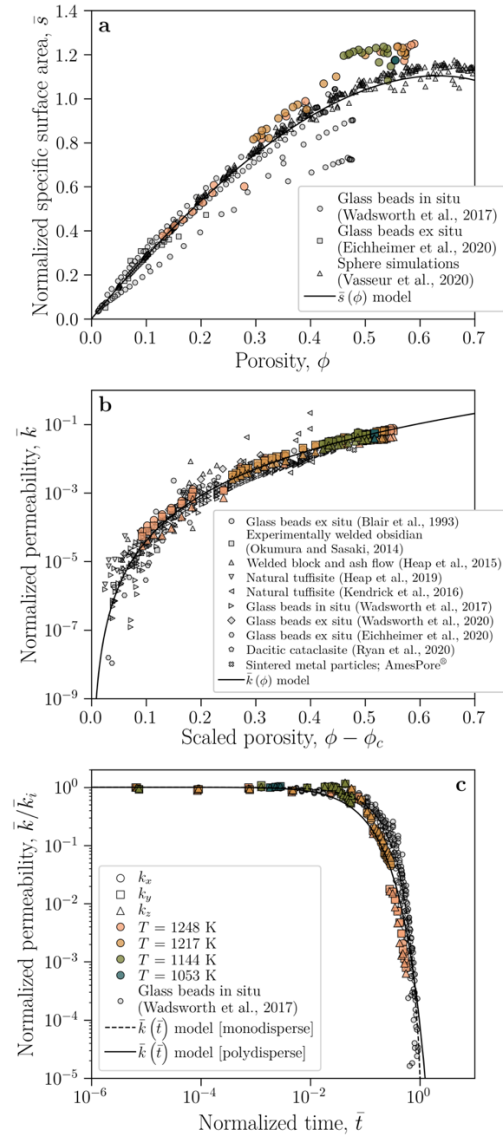


1091

1092 **Figure 6.** The time-evolution of permeability for different isothermal dwell temperatures: (a-b) 1053
 1093 K, (c-d) 1144 K, (e-f) 1217 K, and (g-h) 1248 K; symbols as for Figure 5. The top panels show the
 1094 temperature–time paths; the bottom panels show the associated the permeability–time paths. The range
 1095 of the time axis shown is kept constant for comparison of the timescales involved for different
 1096 temperatures. In the bottom panels we also show the solution to the $k(t)$ model we develop in Section
 1097 2. The solid curves are the coupled model for which the syn-welding degassing of the particles is
 1098 accounted for, while the dashed and dash-dot curves are for the case where the particles are assumed to
 1099 be at the initial or equilibrium H_2O concentration throughout, respectively.

1100

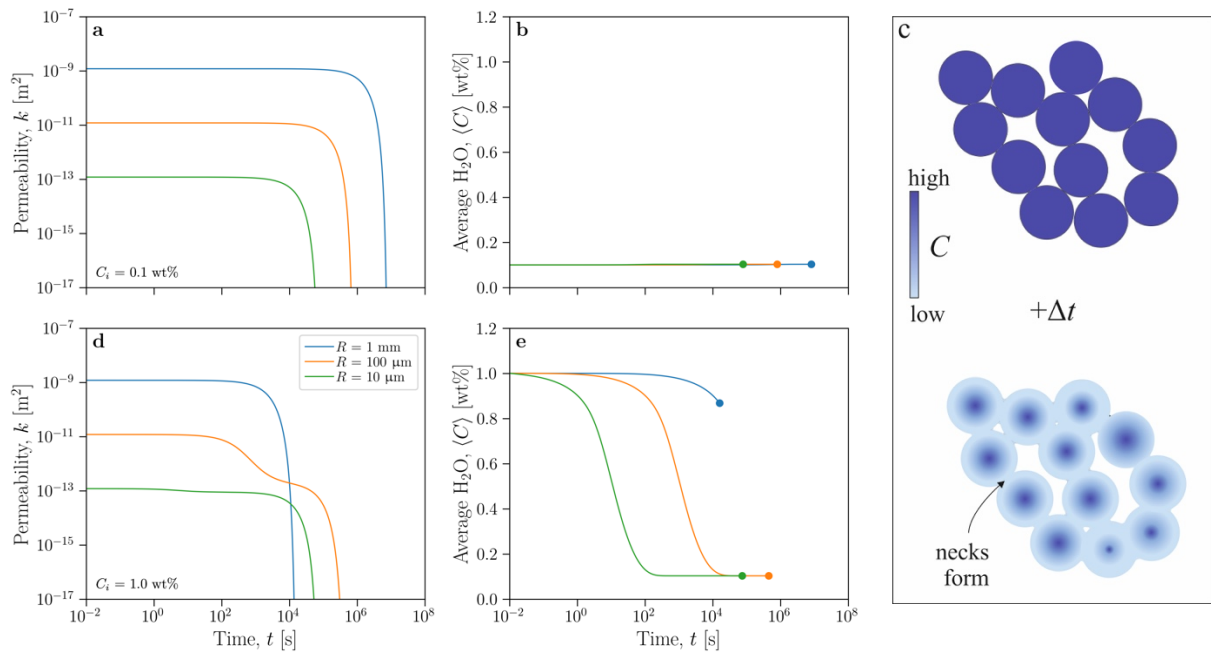
1101



1102

1103 **Figure 7.** The relationships from Figs (4-6) rendered dimensionless and compared with available
 1104 published data. In all panels the data presented in colour are the experimental data from this study (refer
 1105 to panel (c) for the temperatures for each colour). The normalization values for each published dataset
 1106 are given in Table 1. (a) The dimensionless specific surface area as a function of porosity $\bar{s}(\phi)$.
 1107 Additional data shown are for glass bead packs sintered *in situ* (Wadsworth et al. 2017b) and *ex situ*
 1108 (Eichheimer et al. 2020), and for sphere pack simulations (Vasseur et al. 2020). (b) The dimensionless
 1109 permeability as a function of the scaled porosity $\bar{k}(\phi - \phi_c)$. Additional experimental data shown are
 1110 for glass bead packs sintered *in situ* (Wadsworth et al. 2017b) and *ex situ* (Blair et al. 1993; Wadsworth
 1111 et al. 2020b; Eichheimer et al. 2020), for experimentally welded obsidian particles (Okumura and Sasaki
 1112 2014), and for commercially available AmesPore© sintered metal filters (data from:
 1113 <https://amespore.com/en/>). Natural data shown are for welded crystal-poor (Heap et al. 2019) and
 1114 crystal-rich (Kendrick et al. 2016) tuffisites, welded block-and-ash flow deposits (Heap et al. 2015),
 1115 and dacitic volcanic fault gouge (Ryan et al. 2020a). (c) The dimensionless permeability as a function
 1116 of dimensionless time $\bar{k}(\bar{t})$. The curves represent the time-dependent model given in Eq. 2 for $\bar{\phi}(\bar{t})$
 1117 coupled with the $\bar{k}(\phi)$ model. The difference between the solid and the dashed curves arises from the
 1118 definition of a_i for monodisperse (dashed curve) and polydisperse (solid curve) sintering particles. We
 1119 compare our data with previous data for monodisperse sintering glass beads (Wadsworth et al. 2017b).

1120

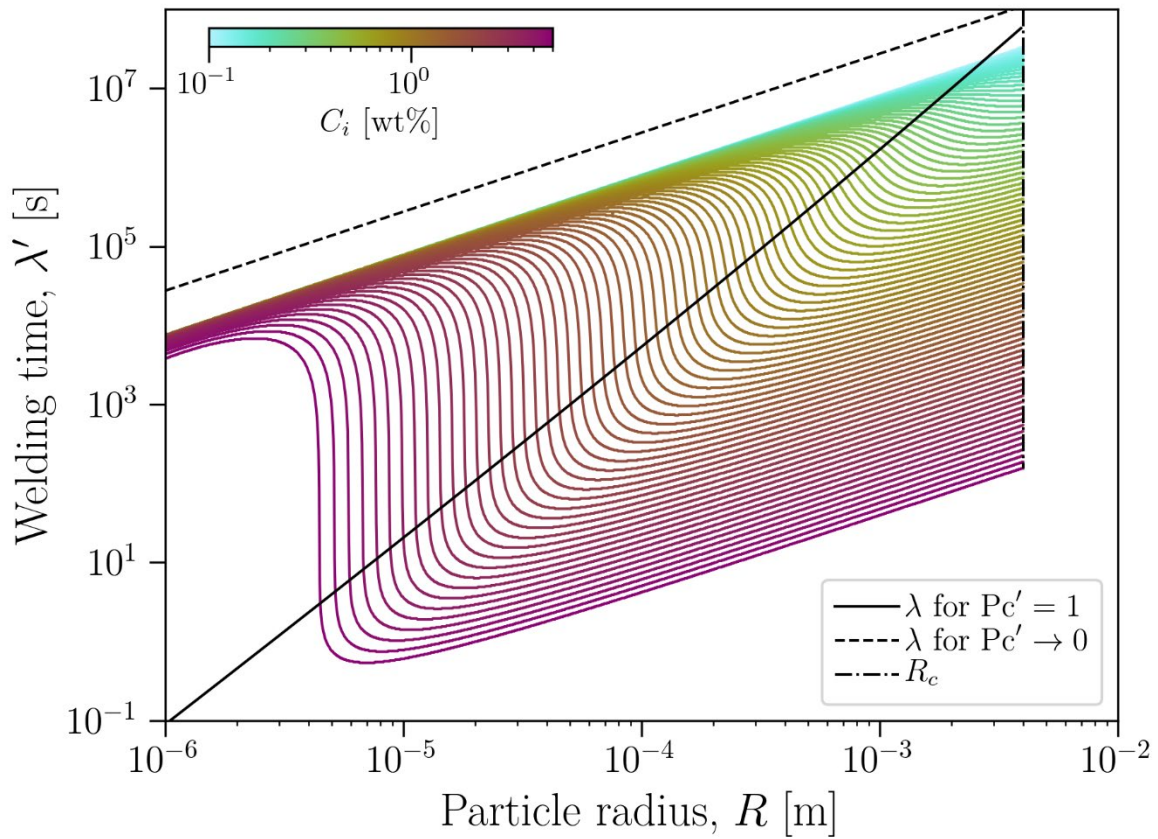


1121

1122 **Figure 8.** Model results for permeability as a function of time $k(t)$ and the average particle H₂O
 1123 concentration as a function of time $\langle C \rangle(t)$ for different particle radius R and initial water concentration
 1124 C_i : (a-b) for $C_i = C_e = 0.1$ wt. %; (c-d) for $C_i = 1$ wt. % and for which C_e is determined at 0.1 MPa.
 1125 In (b) and (d), the filled circle against which the curves terminate represents the time at which welding
 1126 completes λ' . All results are using the $\mu(T, C)$ relationship for rhyolites (Hess and Dingwell 1996) and
 1127 at $T = 1100$ K. c) Schematic cartoon showing the simultaneous evolution of pore-space geometry and
 1128 H₂O distribution in the particle pack, as welding and degassing proceed.

1129

1130



1132

1133

1134

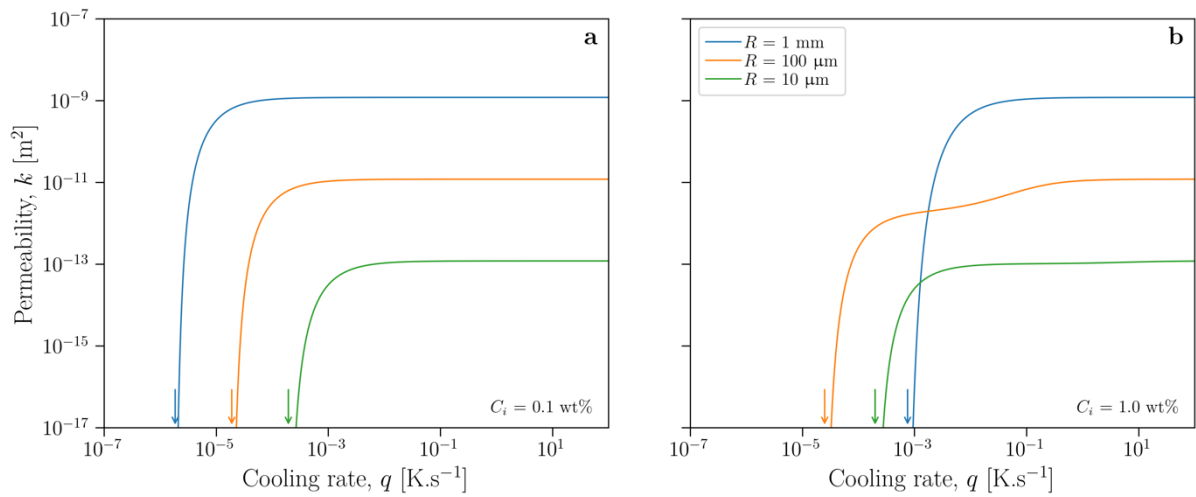
1135

1136

1137

Figure 9. The welding time λ' as a function of the radius R of the welding particles. Model curves are plotted for a wide range of initial H₂O concentration $0.1 < C_i < 5$ wt.%. Models are plotted only for $R < R_c$, such that gravitational effects are unimportant. The low-Pc solution for $\lambda'(R)$ is shown in the dashed line, and the solid line connects the $Pc = 1$ point for each C_i , (i.e. the point where $\lambda = \lambda_D$).

1138



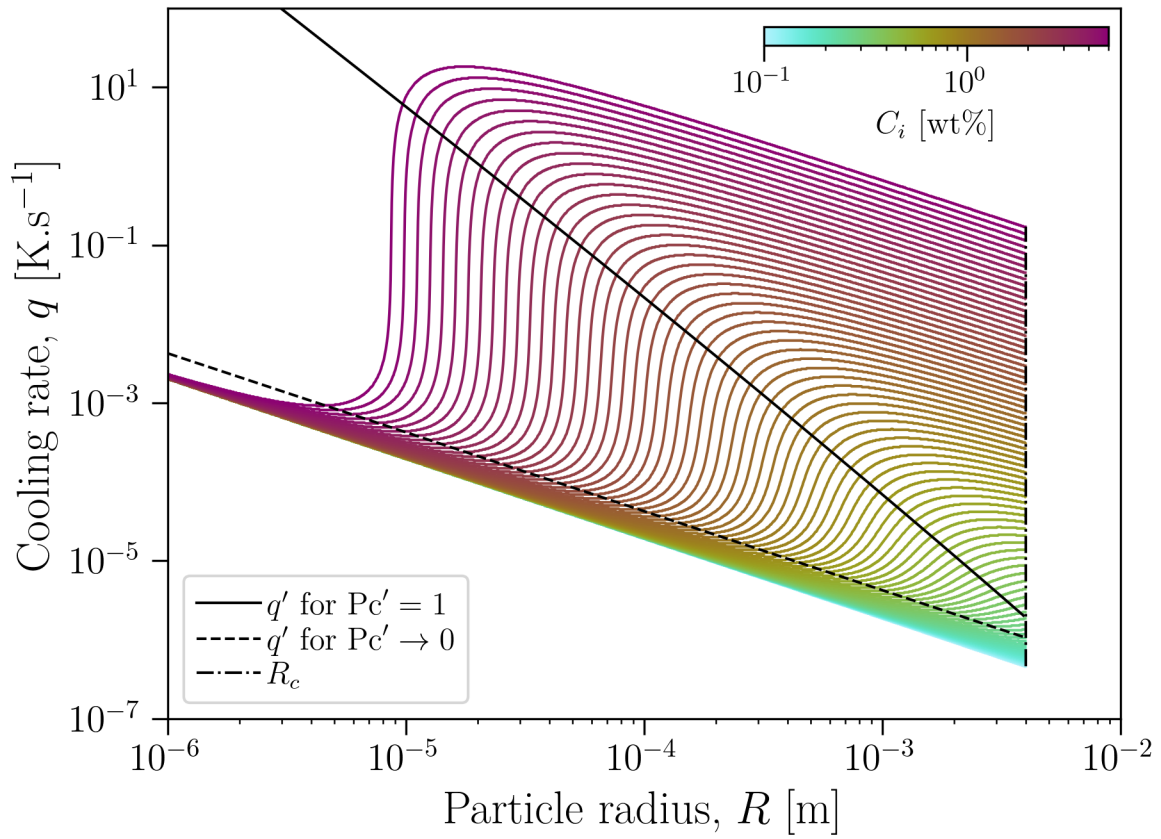
1139

1140 **Figure 10.** The permeability that is preserved in a welding deposit when temperature falls below the
1141 glass transition temperature (i.e. when $T = T_g$) as a function of the cooling rate q . There is a critical
1142 cooling rate q' , below which the permeability falls to zero before T_g is reached (vertical arrows). Results
1143 are shown for (a) low $C_i = 0.1 \text{ wt}\%$ and (b) relatively high $C_i = 1 \text{ wt}\%$. In all cases the equilibrium
1144 H_2O concentration is $C_e = 0.1 \text{ wt}\%$.

1145

1146

1147



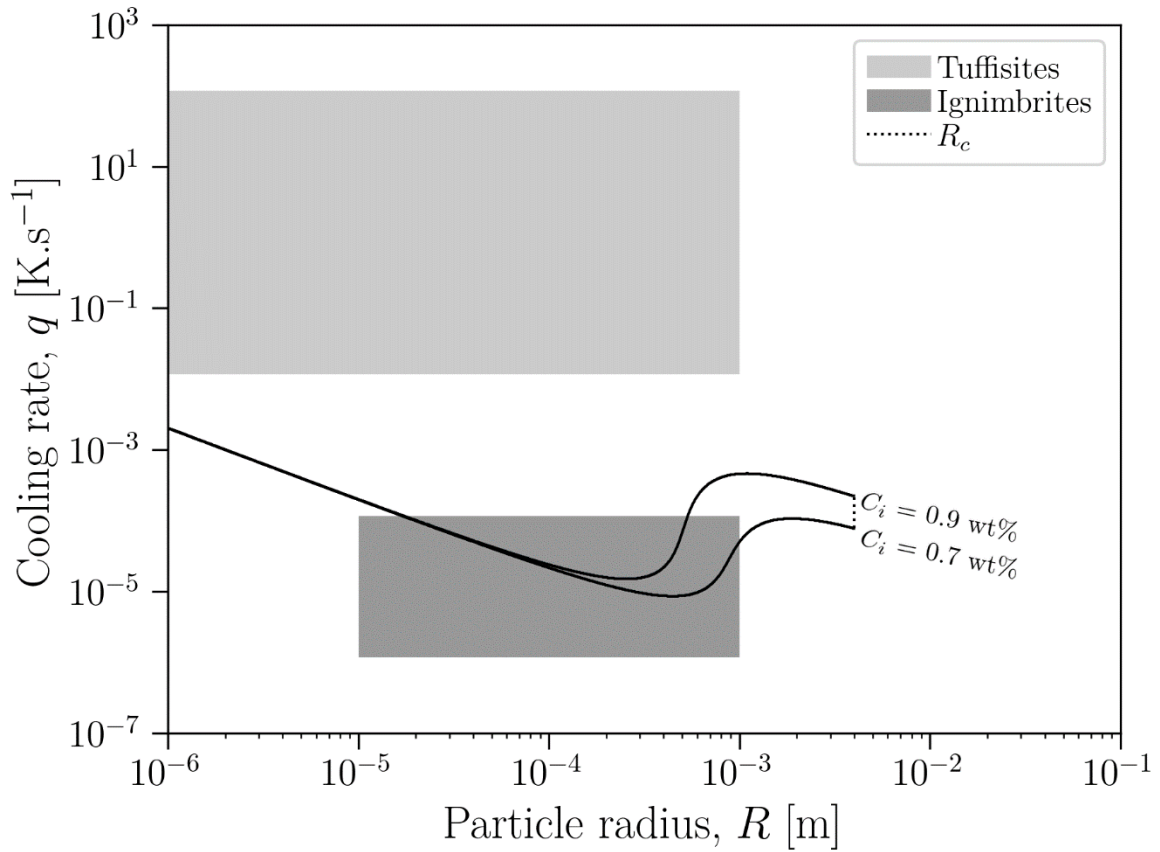
1148

1149 **Figure 11.** The critical cooling rate q' above which welding will not complete and $k > 0$ will be
 1150 preserved in deposits, as a function of R . Model results are shown in colour for a wide range of C_i (see
 1151 Fig. 9). The low- Pc solution for $q'(R)$ is shown in the dashed line, and the solid line connects the $\text{Pc} =$
 1152 1 point for each C_i .

1153

1154

1155



1156

1157 **Figure 12.** Application of our model to natural conditions (see Fig. 1). The model curves show the
 1158 critical cooling rate q' as a function of particle radius R for $C_i = 0.7$ and 0.9 wt.%, typical of the far-
 1159 field value found in obsidian close to tuffisites (Castro et al. 2012; Saubin et al. 2016) and consistent
 1160 with the upper value estimated for natural welded ignimbrites (Sumner and Branney 2002). For a given
 1161 curve, points below the curve represent conditions under which welding completes before the deposit
 1162 quenches; for points above the curve, welding does not complete before the deposit quenches. The box
 1163 shown for tuffisites is bounded by $10^{-6} \leq R \leq 10^{-3}$ m and by q' scaled for tuffisite widths $0.1 \leq L \leq$
 1164 10 cm. The box for ignimbrites is bounded by $10^{-5} \leq R \leq 10^{-3}$ m and by q' scaled for thickness from
 1165 a lower limit of the rising deposition boundary layer in ignimbrites $L = 1$ m to an ignimbrite deposit
 1166 thickness $L = 10$ m. Tuffisites are expected to quench before welding completes, whereas ignimbrites
 1167 may weld fully before quenching.